UC San Diego
UC San Diego Electronic Theses and Dissertations

Title

A robophysical investigation of series-elastic flapping wings

Permalink

Author

Lynch, James Edmund

Publication Date

2019

Peer reviewed|Thesis/dissertation

UNIVERSITY OF CALIFORNIA SAN DIEGO

A robophysical investigation of series-elastic flapping wings

A Thesis submitted in partial satisfaction of the

requirements for the degree Master of Science

in

Engineering Sciences (Mechanical Engineering)

by

James Lynch

Committee in charge:

Professor Nicholas Gravish, Chair
Professor Tom Bewley
Professor Mike Tolley

2019

The Thesis of James Lynch is approved, and it is acceptable in quality and form for publication on microfilm and electronically.

_____

_____

_____

Chair

University of California San Diego

2019

TABLE OF CONTENTS

LIST OF FIGURES

LIST OF TABLES

ACKNOWLEDGEMENTS

This report represents the culmination of nearly two years of hard work, but it could not exist without the support of so many others.

To my advisor, Professor Nicholas Gravish: thank you for your constant encouragement, creativity, and guidance. When I was lost in the weeds, sifting through data and trying to make sense of what was there, you motivated me to press on and brought out my best work. I look forward to all our future collaborations.

To our collaborators, Jeff Gau and Professor Simon Sponberg: our weekly meetings were invaluable in teaching me how to talk about my project and present results in a way that was clear, focused, and relevant. You helped me to chisel out some direct questions from a broad idea and craft a compelling message while providing context that would have otherwise been inaccessible.

To my committee members, Professors Tolley and Bewley: thank you for your ongoing support and for your advice and fresh perspectives on the project.

To Dennis Wu: the work you did to get the ball rolling on the series-elastic wing apparatus made it possible for me to spend the time I needed on understanding the data it produced. Without that, I might still be troubleshooting. Thank you!

To the members of the Gravish Lab: thank you for all the excellent conversation, great ideas, and fun times in and out of the lab. It is hard to imagine how I would have gotten through the challenges of this project without your support and friendship.

Finally, to my friends and family: thank you for your unending encouragement and love throughout these challenging and rewarding couple of years. I couldn't have done it without you.

ABSTRACT OF THE THESIS

A robophysical investigation of series-elastic flapping wings

by

James Lynch

Master of Science in Engineering Sciences (Mechanical Engineering)

University of California San Diego, 2019

Professor Nicholas G. Gravish, Chair

Flying insects may achieve energy efficient flight by storing and releasing elastic energy in their thorax, tendons, and muscle. Similarly, flapping wing micro-aerial vehicles (FWMAVs) may benefit from the inclusion of elastic components in their actuation system. Despite significant investigation into the aerodynamics of flapping wings, the actuation of these movements through elastic structures in insects and robots is relatively unexplored. We have developed a dynamically-scaled robophysical experiment to study the dynamics of series-elastic flapping wings, with specific emphasis on discovering the role of linear and nonlinear elastic components in energy efficiency, perturbation resistance, and control. We vary system (inertia

and elasticity) and actuation (amplitude and frequency) parameters and find that energy storage and recovery by an elastic element is dependent on the stiffness of the element, the inertia of the system, and upon the driving amplitude and frequency. Experimental results are compared to the results of an analysis of a simplified model of the system. The comparison suggests that an effective model of elastic flapping wings must account for unsteady aerodynamic mechanisms that arise from the flow about the oscillating wing. The same experiments suggest that the inclusion of series-elastic elements may have a negative overall effect on control capabilities. The results of the project will inform the design of future FWMAVs, providing insight in elastic element selection, power requirements, and control design as well as addressing open questions in biology about actuation and control in flying insects.

CHAPTER 1: INTRODUCTION & BACKGROUND

Flapping wing flight is characterized by large power requirements, as actuators must provide enough power to generate aerodynamic forces while overcoming inertial acceleration of the wing during flapping motion. Despite this, flying insects have been incredibly successful since first evolving wings over 300 million years ago, demonstrating unparalleled agility as well as impressive long-range flight capabilities [1], [2]. In the last two decades, roboticists have taken inspiration from the success of flying insects – and other agile fliers, like hummingbirds – to develop flapping wing micro-aerial vehicles (FWMAVs) at the centimeter scale and smaller. Several examples, including the Harvard Robobee [3], [4], the Delfly [5], the AeroVironment Nano Hummingbird [6], and the COLIBRI flying robot from Université Libre de Bruxelles [7], have demonstrated controlled flight using a variety of actuation and control schemes (Fig. 1.1).
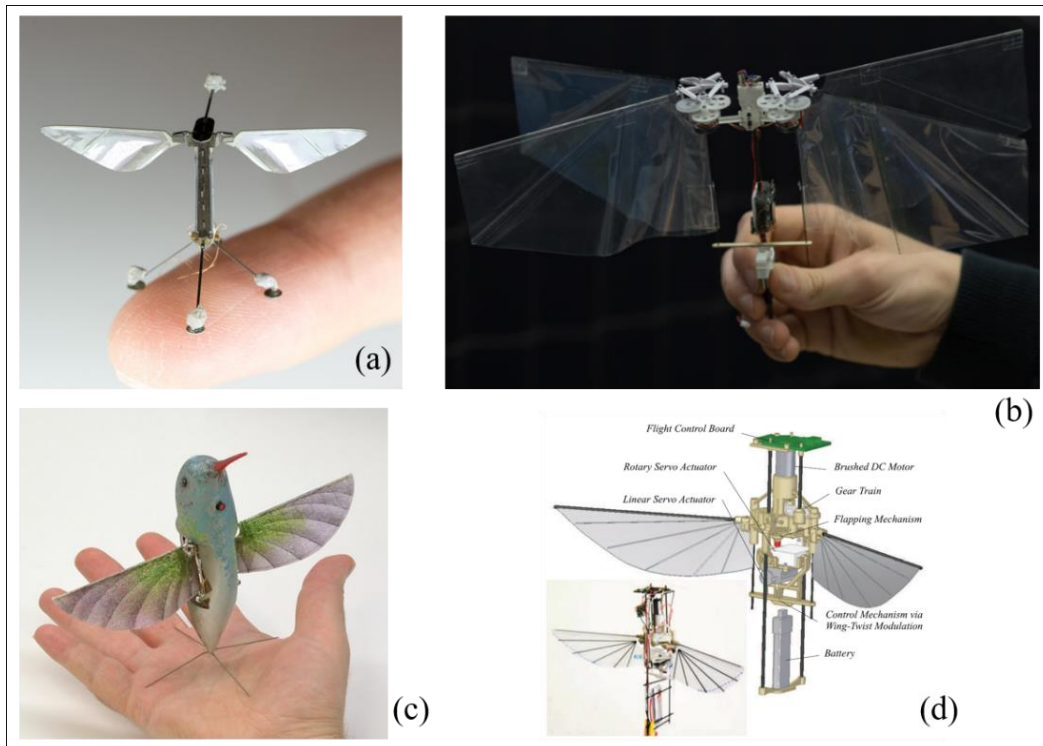
Figure 1.1: Examples of flapping wing robots (a) The Harvard Robobee [4] (b) The Delfly Nimble [5] (c) The AeroVironment Nano Hummingbird [6] (d) COLIBRI [7]

Still, a major challenge facing designers of FWMAVs is achieving efficient flight. The Robobee must be tethered to a ground-based power supply, and flight times for un-tethered MAVs is short (< 8 minutes). This problem will be especially pressing as designers seek to further miniaturize and add useful payloads like cameras and sensors.

1.1: Resonance & Elasticity in Insects

Insects demonstrate superior aerodynamic efficiency despite the high power requirements inherent to flapping wing flight at intermediate Reynolds numbers. The prevailing theory of the last half-century is that insects achieve efficient flight by operating at or near resonance; that is, they flap their wings at frequency that closely matches the natural frequency of a spring-mass system with the insect's effective inertia and stiffness [8]–[10]. Resonance allows fliers to store some energy in compliant elements of the wing "transmission" during the forward stroke which can then be returned during the back stroke, reducing the cycle-averaged power expended by the
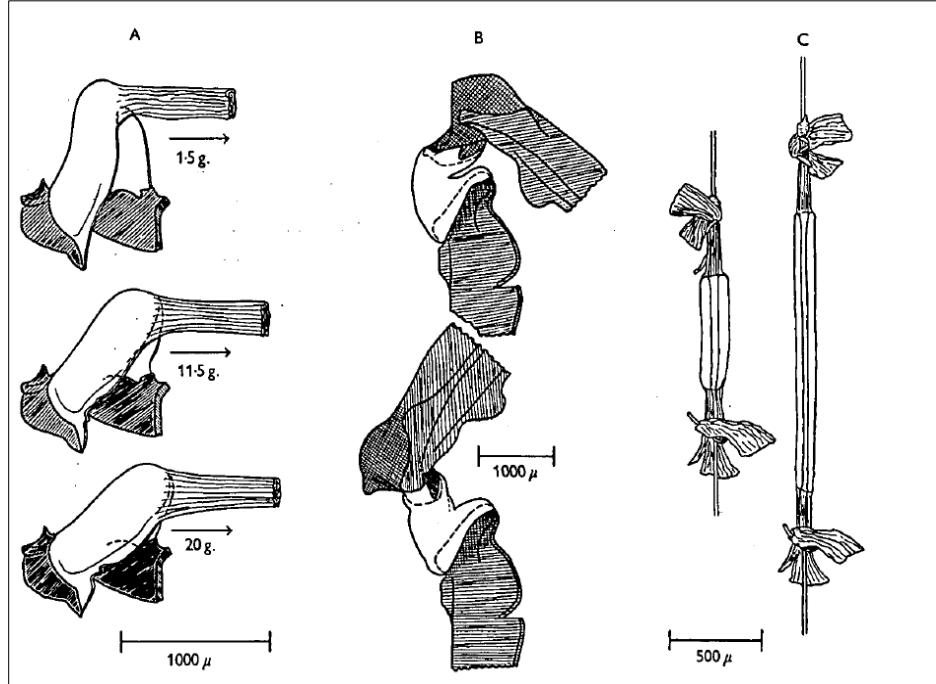
Figure 1.2: Three examples of resilin structures from insect thoraxes. (A) the prealar arm from a locust (*Schistocerca*) strained by three different loads. (B) The main wing hinge of a locust forewing, unstrained (above) and strained (below). (C) The elastic tendon of a dragonfly (*Aeschna*) unstrained and extended. The parts shown in white consist mainly or entirely of resilin. From [11].

insect muscle. This energy storage is made possible by the presence of resilin – a highly elastic, rubberlike protein – in the thorax, joints, and tendons of flying insects.

The insect cuticle, which includes most of the material of the exoskeleton, is complex and varies significantly in structure and composition between species and even between individuals. Much of it is dominated by materials that may be characterized as rigid at the insect scale, but the exoskeletons of many insects also include patches of a rubber-like protein known as resilin. Resilin was first described in 1960 by Torkel Weis-Fogh [11], who pointed out its role in the elastic tendons of dragonflies and wing hinges of desert locusts (Fig. 1.2). He also noted that resilin structures had the ability to snap back after deformation, even after been strained over long periods of time. Later, Jensen and Weis-Fogh performed a suite of dynamic tests of the elastic structures of locusts and found that the energy loss due to damping was under 5% even at frequencies as high as 200 Hz [12]. The lack of energy loss even at such high frequencies suggests that resilin is near-perfectly elastic, ideal for energy storage at the high frequencies characteristic of insect flight. Others would go on to identify resilin structures in the springs that power the high-speed catapult used by jumping fleas, the folding mechanisms of earwig wings, and the high-frequency sound-producing mechanism of cicadas [13]. The importance of resilin in flapping wing flight arises from the ways that elastic elements of insect anatomy are arranged in series and in parallel with muscles.

Flying insect morphology can be broadly divided into two categories: 1) direct flight morphology in which groups of muscles apply force directly to the wing joint, and 2) indirect flight morphology in which a pair of antagonistic muscles apply force to the thorax which consequently deforms and deflects the wing hinge (Fig. 1.3) [14]. In direct flight mechanisms,

resilin is found in elastic tendons and in the wing hinge itself. Indirect mechanisms also incorporate resilin wing hinges, but resilin patches are also found in the thorax, enabling energy storage via thorax deformation. Many advanced insects, like flies and bees, incorporate both direct and indirect flight morphologies, using indirect muscles to power flight and direct muscles to control wing orientation.
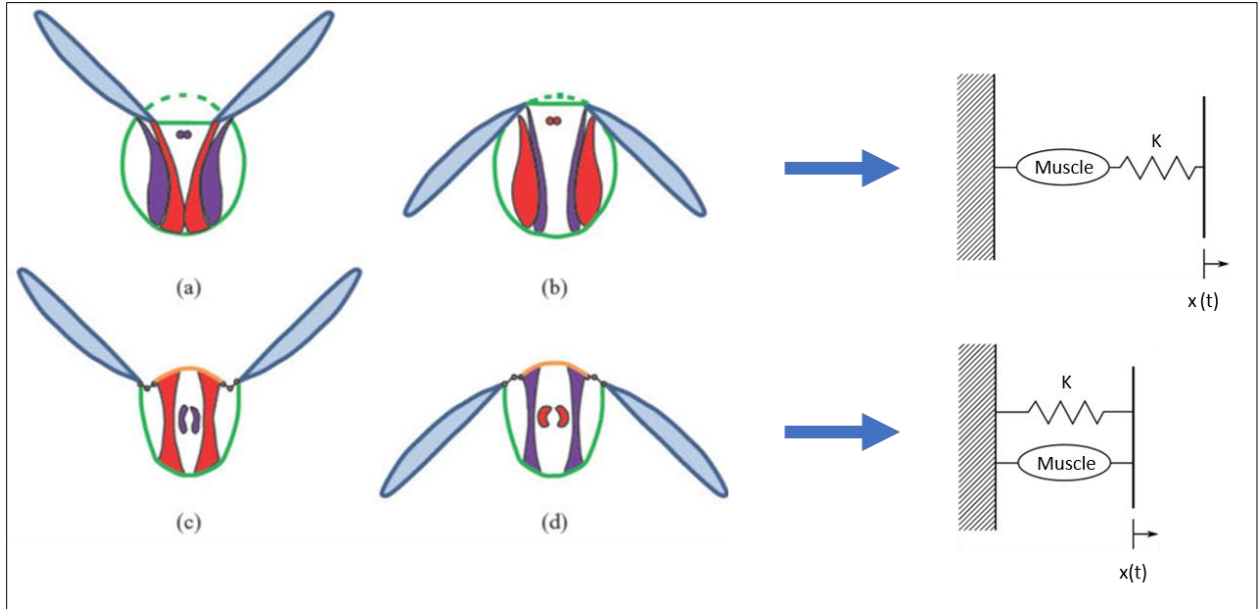
Figure 1.3: Diagrams of the cross-section of insect thorax mechanisms used for flight. (a) and (b) depict the upstroke and downstroke, respectively, in thoraxes with direct flight morphologies. From a dynamical perspective, this mechanism is analogous to a *series-elastic* oscillator. (c) and (d) depict the upstroke and downstroke in those with indirect flight morphologies. This mechanism is analogous to a *parallel elastic* oscillator. Red muscles indicate muscles in tension, and the flexible portion of the thorax that transmits force to the wing is show in orange. Adapted from Zhang & Rossi [14]

The integration of elastic components in direct and indirect insect flight morphologies suggests that the wing transmission may be modelled as a complex system of parallel and series springs which has a resonant frequency that depends on the compliance and inertia of the system. A representative diagram is provided in Figure 1.4. Muscle actuated at the resonant frequency will need to do only positive work to overcome drag while the springs take on the entirety of the inertial load [15], [16]. This suggests that aerodynamic efficiency is optimal at this resonant

frequency, which is further supported by the observation that many insects flap their wings within a narrow range of frequencies[17], [18].
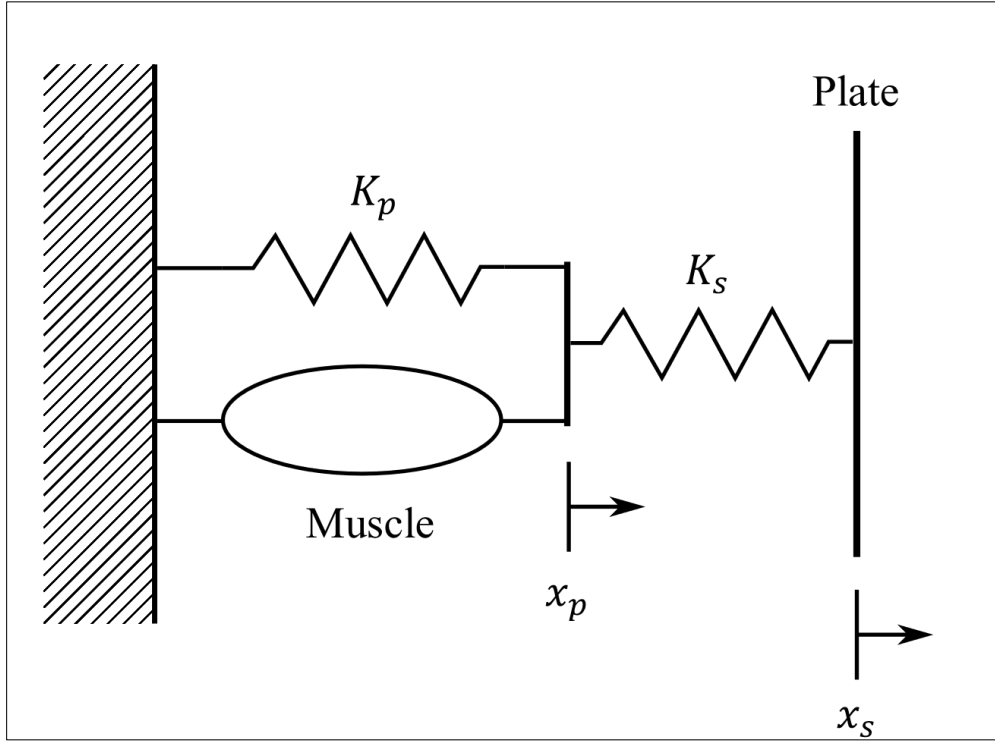
Figure 1.4: Model of insect thorax with series and parallel elasticity. K_p and K_s represent the stiffness of elastic elements in parallel and in series with muscles, respectively. Both the muscle and the parallel spring are subject to displacement x_p, while the series spring is deflected by the difference between x_s and x_p.

1.2: Resonance & Elasticity in Flapping Wing Micro-Air Vehicles

Inspired by the elasticity of flying insect morphology and seeking to take advantage of the energy-saving properties of resonant systems, some designers have integrated elastic elements into flapping wing systems. Zhang & Rossi conducted a thorough review of such compliant flapping wing mechanisms [14] and discussed various methods of implementing elasticity in flapping wing systems.

Some examples, like a prototype flapping wing MAV from CMU [19] and a flapping wing mechanism from UC Berkeley [20], used DC motors in parallel with metal springs to drive their wings (Fig 1.5). Both studies found benefits to integrating compliance: the Berkeley team

reported a reduction of average power of up to 30%, and the CMU MAV demonstrated liftoff

and a maximum lift-to-weight ratio at the resonant frequency. However, the addition of metal

springs to the system added weight and did not reduce losses due to joint friction, suggesting that

integrating compliance directly into the mechanism might be preferable.
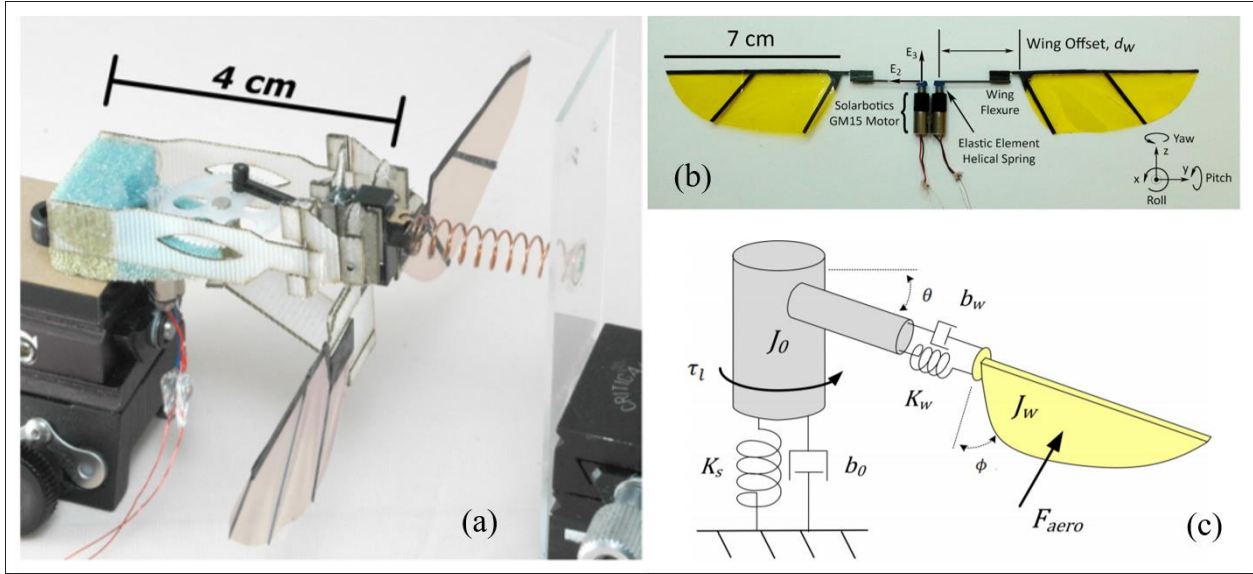
Figure 1.5: Flapping wing systems with DC motors and metal springs. (a) A 5.8 gram flapping
mechanism with linear spring and DC motor-driven piston developed at UC Berkeley [20]. A photo (b)
and simplified diagram (c) of a prototype flapping-wing micro-air vehicle [19].

To that end, other groups developed flapping wing mechanisms that transmitted power

from a DC motor to the wings via a compliant frame, much like the compliant thorax of an

insect. Sahai et al [21] integrated rubber-based flexures into the joins of an otherwise rigid

transmission and found that the mechanism saved up to 20% of input power and produced more

thrust than a rigid transmission for the same input. Researchers at UMD developed two

compliant frames for their Small Bird and Jumbo Bird MAVs [22]. The Small Bird used a frame

manufactured in one, injection-molded piece that reduced the weight and improved the

efficiency of the transmission. For the Jumbo Bird, the designers utilized a multi-material

fabrication method to create a frame with rigid links coupled to compliant hinges, which also demonstrated improved efficiency.

At small scales, DC motors become inefficient, so the smallest FWMAVs must use another method of actuation. Perhaps the most successful sub-centimeter scale FWMAV, the Robobee (Fig. 1.6), uses piezoelectric bending actuators and a transmission constructed from lightweight polyamide film and carbon-fiber-reinforced polymer to achieve controlled flight [3]. The transmission was fabricated via a method of laser-micromachining and lamination of different materials in 2D that could then be folded into 3D geometries. The flight of the Robobee, whose compliance comes from both the use of polyamide hinges in a carbon fiber transmission as well as the inherent elasticity of the piezoelectric actuators, relies on resonance of the system to achieve maximum lift and aerodynamic efficiency. Flight control was achieved by varying wing amplitude, relative phase, and center of oscillation, but frequency was held at 120 Hz because of the significant drop off in lift away from the resonant frequency.
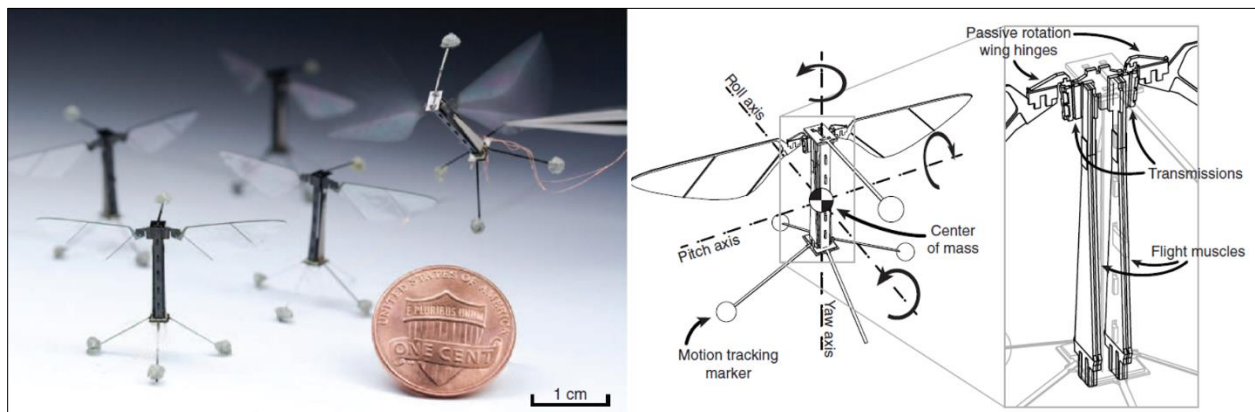
Figure 1.6: The Harvard Robobee. (left) Photo of the Robobee. (right) A diagram showing the composite frame, piezoelectric "flight muscles," and folded compliant transmission of the Robobee [3]

As evidenced by the success of the designs detailed above, compliant transmissions improve performance and enable flight even at very small scales. However, they present only part of the picture when it comes to compliant flapping wing systems. Each example of a

compliant flapping wing mechanism above incorporates only *parallel* elasticity. Insect flight morphology is characterized by both parallel and *series* elasticity, and therefore there are elements of the dynamics of such systems that have not yet been studied.

In a parallel elastic configuration, the actuator and spring are constrained such that they always have an equivalent deflection. The spring exerts a correcting force that pushes the motor back to the neutral position, and, at resonance, the storage and release of energy leads to a minimization of the power required to move the wing. In the series-elastic case, the motor and spring are subject not to a kinematic constraint, but a *dynamic* one. The motor and spring are subject to the same force, but they do not share the same kinematics. The kinematics of the wing depend on a combination of actuation input, system stiffness and inertia, and aerodynamic loading. As such, analysis of a series-elastic system requires consideration not only of the mechanics of the wing, but also of the aerodynamic mechanisms that dictate the forces on the wing.

1.3: Aerodynamics of Flapping Wing Flight

The aerodynamics of flapping wing systems in nature have been studied extensively. As better methods of observing and recording the wing kinematics of such fliers improved in the mid-20th century, researchers began to propose models for understanding the aerodynamic mechanisms at play. Early studies suggested that a relatively simple, quasi-steady model could account for the dynamics observed, but it is now believed that unsteady fluid behavior (induced vortices, added mass, and wing-wake interaction) play a major role. The following section will discuss the factors that contribute to flapping wing aerodynamics.

1.3.1: The Quasi-Steady Model

The *quasi-steady assumption* refers to the hypothesis that the instantaneous forces on a flapping wing are those corresponding to steady motion at the same instantaneous velocity and attitude. Therefore, if the kinematics and geometry of the wing and the properties of the surrounding fluid are known, one should be able to compute the forces experienced by the wing. Coupled with blade-element theory, it becomes possible to resolve the force, F', on a wing element into lift, L', and drag, D', components:

$$F' = \sqrt{L'^2 + D'^2}$$

$$L' = \frac{1}{2}\rho c U_r^2 C_L(\alpha) = F'\cos(\alpha)$$

$$D' = \frac{1}{2}\rho c U_r^2 C_D(\alpha) = F'\sin(\alpha)$$

where ρ is the mass density of the fluid, c is the wing chord, U_r is the relative velocity perpendicular to the wing axis, and α is the wing pitch angle. Integrating along the span of the wing gives the total force on the wing, which is proportional to the square of the velocity of the wing. Applications of this model also assume that, while the coefficients of drag and lift likely vary over a stroke, the variation is small enough that the mean coefficients over a stroke are sufficiently reliable.

The only real way to validate the quasi-steady model of flapping wing flight is via proof-by-contradiction. Once the kinematics of a certain insect (or robot) are collected, the mean forces generated by the wings may be calculated. If those forces do not satisfy the net force balance of a flier, then it can be argued that the assumption must be false. This is the approach applied by Weis-Fogh, who found that the quasi-steady assumption was valid for hovering in hummingbirds and flies [23], [24]. However, Ellington, in his six-part treatise on the aerodynamics of hovering

insect flight [25]–[30], came to the opposite conclusion. His observations suggested that during

hovering, when the *reduced frequency*, given by

$$\kappa = \frac{\omega \times b}{V}$$

where ω is the circular frequency, b is the airfoil semi-chord, and V is the flow velocity,

approaches infinity, unsteady features of the flow contribute significantly to the net forces on the

wings. He argued that the quasi-steady assumption is *not* sufficient to describe the aerodynamics

of flapping wings and described unsteady effects that could contribute to the net forces. Since his

seminal publication, many others have continued to examine those factors, some of which will be

discussed in the following sections.

1.3.2 Unsteady Aerodynamic Mechanisms in Flapping Wing Flight

Five primary mechanisms have been identified to explain how insects generate

aerodynamic forces with their wings: added mass, delayed stall due to a strong leading-edge

vortex (LEV), rotational circulation, wing-wing interactions ("clap-and-fling"), and wing-wake

 interactions. Combined with the quasi-steady assumption provided above, these mechanisms

provide a strong model for the aerodynamics of flapping wing insect flight [31].

1.3.2.1: Added Mass

The insect wing stroke consists of an upstroke, downstroke, and two reversal periods (supination

and pronation) that ensure that the leading edge of the wing always leads (i.e. it maintains a

positive angle of attack). When the insect decelerates its wing in order to reverse direction, it

must also decelerate the air closest to the wing. This results in an additional force on the wing

that is experienced as an additional wing mass by the flapping wing structure (Fig. 1.7 A, E). The

effect is therefore referred to as "added mass" and can be modeled as a time-varying inertia that

spikes at reversal, resulting in augmented aerodynamic force generation.
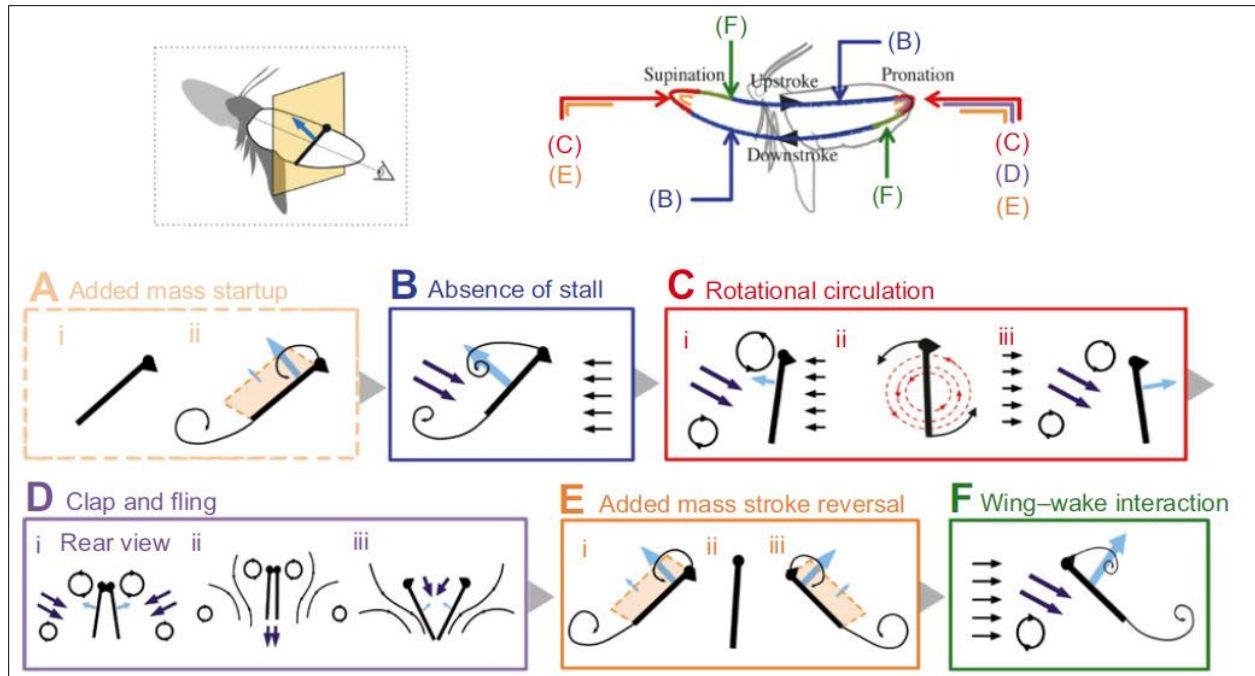
Figure 1.7: Overview of Aerodynamic Mechanisms in Flapping Wing Flight. (A) When starting up, the insect must overcome the added mass effect caused by the surrounding air. (B) During the mid-stroke of the wing trajectory, a strong, stable leading edge vortex is formed, greatly enhancing lift and preventing stall. (C) At reversal, the timing and duration of wing rotation can have significant effects on lift, drag, and flight efficiency. (D) Interactions between wings, such as the "clap-and-fling" mechanism shown here, can augment lift by creating an area of low pressure between the wings, above the insect. (E) Added mass also has an influence during reversal, when the insect must decelerate and accelerate the fluid closest to the wing. (F) After reversal, the wing sweeps back through the flow induced by the last semi-stroke, increasing the relative velocity of the fluid with respect to the wing, augmenting the lift/drag experienced by the wing. In all figures, the wing is drawn in black with the leading edge designated by a circle. The diagram in the upper right indicates at which point during the wing stroke each mechanism is active. Figures adapted from [31].

1.3.2.2: Delayed Stall and LEV

During flapping at high angle of attack, the air flow separates at the leading edge, and the separated boundary layer rolls into a strong leading-edge vortex (LEV) that remains stably attached to the wing during the wing stroke (Fig. 1.7 B). In 2D translation, such a vortex would be expected to grow larger until it can no longer remain attached to the wing, causing the flow to separate and the vortex to shed and form a von Karman street. However, in 3D wing rotation, Coriolis accelerations cause momentum to be transferred in the spanwise directions, creating a helical vortex that enhances lift (and drag) on the wing and remains attached to the wing

11

throughout the wing stroke [32]. This mechanism is thought to be the primary source of lift augmentation in the mid-stroke.

1.3.2.3: Rotational Circulation

During reversal, the wing rotates so that the insect always maintains a positive angle of attack. Sane and Dickinson studied the influence wing rotation has on lift and drag via a dynamically scaled model insect [1], [33], [34]. They found that due to the Kramer effect, a phenomenon in which a rotating wing induces rotation in the surrounding fluid, wing rotation has a significant effect on the lift and drag experienced by the wing during the wing stroke (Fig. 1.7 C). In hovering flight, these effects contribute up to 35% of lift in a robotic model of a fruit fly and 50% of lift in a robotic model hoverfly [1]. Note, however, that these values may not be quantitatively accurate because of the limitations of using such a scaled robotic model.

1.3.2.4: The Clap-and-Fling Mechanism

First proposed by Weis-Fogh [24] to explain high lift in tiny flying insects, clap-and-fling is a mechanism that some insects use to magnify the lift they generate (Fig. 1.7 D).. In clap-and-fling, an insect's wing amplitude is large enough that its wings meet ('clap') at the top of the upstroke, expelling a jet of fluid from the trailing edge. When the wing stroke reverses, the leading edges of the wings peel off while the trailing edge remains attached, creating a low-pressure region between them and inducing opposite vortices on each wing as it translates ('fling'). This mechanism leads to higher lift, but considering that it is relatively uncommon in flying insects, the effect may be fairly small [32]. It also may be explained as a result of a need to increase wing stroke amplitude to the mechanical limits of the insects, which is also desirable for maximum lift.

1.3.2.5: Wing-Wake Interactions

Following stroke reversal, a flapping wing can recover some energy lost to the fluid by "capturing" vorticity from the wake induced by the previous semi-stroke (Fig. 1.7 E). Dickinson observed that this results in a peak in aerodynamic forces immediately following stroke reversal. This so called "wake capture" mechanism may contribute as much as 25% of total lift during hovering, an effect that increases with larger amplitudes [34]. The phenomenon is, however, difficult to measure directly. Dickinson used particle image velocimetry to create images that show significant wake induced by the previous stroke and estimated the magnitude by observing the differences between measured forces and wing acceleration effects [1], [34].

1.4: Summary & The Robophysical Approach

Evidence suggests that the elasticity of insect wing transmissions enables more efficient flight via dynamic energy storage and return during flight. This is further supported by findings by roboticists that suggest that compliant transmissions in flying robots result in energy savings and higher thrust. However, most implementations of compliance have been in *parallel* with the actuation method, not in *series*. Insects have examples of *both* series and parallel elasticity in their wing transmission, so a better understanding of the influence of series-compliance on the dynamics of flapping wing systems is necessary to understand the overall dynamics and control of compliant flapping wing systems.

We have designed a dynamically scaled, robophysical model of a series-elastic flapping wing transmission in order to investigate the influence of aerodynamic forces, system parameters like inertia and stiffness, and actuation input on the dynamics of such systems. The robophysical approach to the study of flapping wings is not new; Dickinson used a scaled-up "RoboFly"

immersed in mineral oil to study forces on the wings of flying insects, and Ellington used a 10-times scaled flapper in air for flow visualization (Figure 1.8) [1], [35].
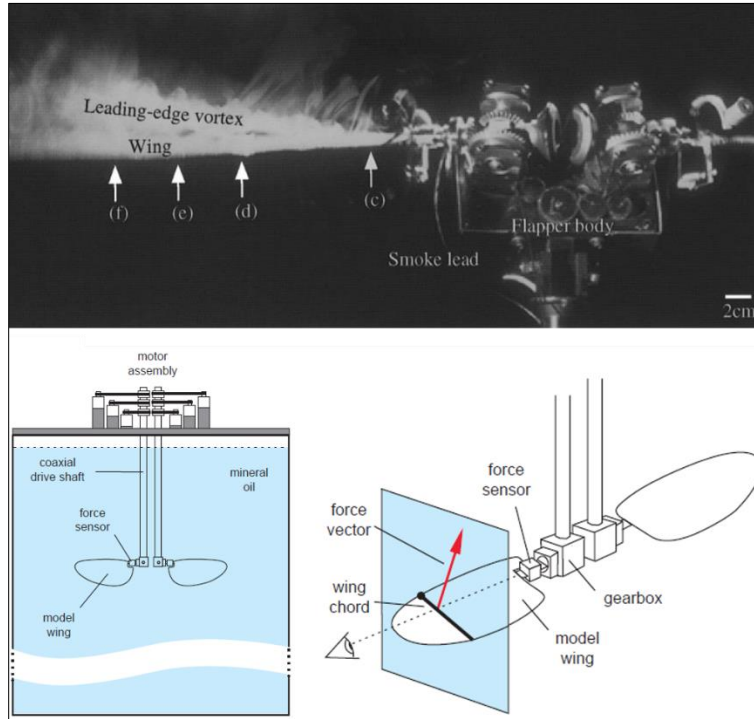
Figure 1.8: Other robophysical studies of flapping wings (top) C. van den Berg & C. P. Ellington used a 10x scaled flapping wing modeled after the hawkmoth (*Manduca Sexta*) for visualization of LEVs in air. [35] (bottom) Dickinson et al. performed dynamically-scaled experiments in mineral oil with a flapping wing model equipped with force sensors in an effort to characterize the aerodynamic mechanisms involved in insect flight [1].

However, both studies incorporated *rigid* transmissions so they could directly control the kinematics of the wing through the fluid. In our series-compliant transmission, the wing kinematics are a cumulative result of the interactions between the mechanical system and the fluid through which the wing moves. We seek to investigate how series-compliance influences the dynamics and control of flapping wing systems by characterizing the design parameter space.

This thesis will detail the design and implementation of a dynamically scaled, series-elastic robophysical system. It will then discuss the results of a first project that seeks to test the hypothesis that unsteady aerodynamic mechanisms including wing-wake interactions and added mass have a significant effect on the dynamics of series-elastic flapping wing system.

Experimental results will be compared to those of a lower-order analysis of series-elastic systems and the differences between them will be discussed.

CHAPTER 2: METHODS & EXPERIMENT DESIGN

In order to study the dynamics of series-elastic flapping wings, we propose a simplified model of such systems and construct a dynamically-scaled robophysical analogue. We perform a range of experiments to evaluate the effects of varying motor input trajectory and physical system parameters on the wing trajectory and energetics of the wing transmission. Specifically, we track the trajectory of the wing induced by inputs with various amplitudes and frequencies to reveal features of the entire parameter space.

2.1 Simplified Model of a Series-Elastic Wing
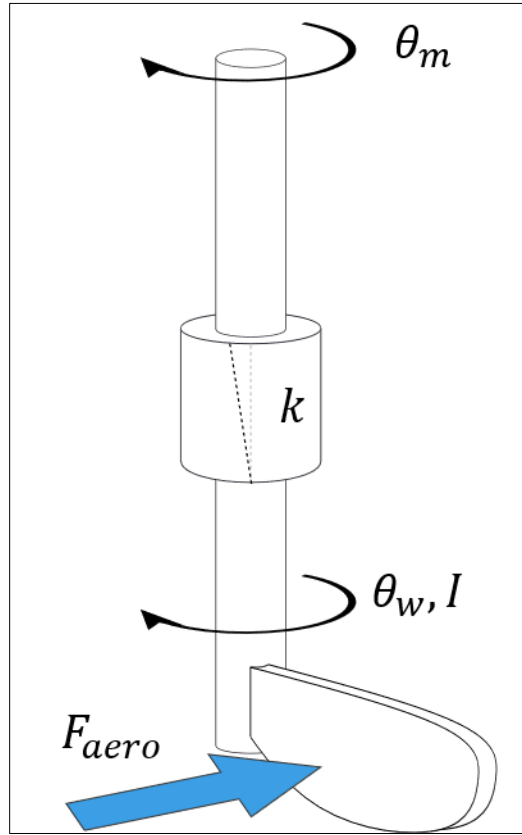
Figure 2.1: Simplified system diagram

As discussed in Chapter 1, evidence suggests that insects store energy in a compliant thorax, elastic tendons, and elastic wing hinges in order to achieve improved flight efficiency. Exactly how energy is distributed across elastic regions of an insect's anatomy is not yet fully

understood, so attempting to precisely mimic an insect here is unrealistic. Instead, we choose to isolate the series-elastic dynamics of the wing transmission in order to study their contributions to overall wing dynamics. We model the behavior of muscle contractile elements as a prescribed displacement and the sum of the elastic proteins in tendons and joints as a single elastic element.

The diagram in Figure 2.1 represents the simplified model of the robophysical system. It is a forced harmonic oscillator subject to nonlinear fluid damping forces and consists of a rotating mass with constant inertia I, a torsion spring with stiffness K, and an aerodynamic drag force F_{aero}. Assuming the load on the wing is quasi-steady with a constant coefficient of drag, C, its equation of motion is

$$I\ddot{\theta}_w = K(\theta_m - \theta_w) - C\dot{\theta}_w^{\ 2} \tag{2.1}$$

The motor angle, θ_m, is the input to the system, and will be a sinusoid with amplitude A_m and frequency ω:

$$\theta_m = A_m \sin(\omega t) \tag{2.2}$$

By choosing an explicit input displacement over an explicit input force, we are able to decouple the dynamics of the series-elastic system from the dynamics of the motor. This simplifies the analysis of the system and allows us to focus on the effects of the stiffness and aerodynamic force terms in the governing equations. However, this choice requires that our robophysical system must use a motor that has a high enough continuous torque that its dynamics are significantly faster than those of the wing/spring assembly. Motor selection is addressed in detail in Section 2.3.

2.2 Dynamic Scaling

In order to make this investigation relevant to micro-robotic and biomechanical interests, it is important that the system be properly scaled. The kinematics and geometry of a flapping

wing can significantly affect the formation of fluid structures (boundary layers, LEVs, etc.) about the wing and therefore affect the fluid forces on the wing. Thus, it is important that the robophysical system operate in the same Reynolds number regime as the biological and robotic systems [31], [36]. Insects typically fly in the range of $Re = 10^2 - 10^4$, so we seek to design a robophysical system that operates in a similar range but at a larger scale. Reynolds number for a flapping wing is a function of the mean velocity of the wing tip, $\bar{U}$; the mean chord length, c; and the kinematic viscosity of the fluid, v:

$$Re = \frac{\bar{U}c}{v} \tag{2.3}$$

The mean velocity of the wingtip (assuming sinusoidal motion of the wing) is

$$\bar{U} = \frac{L\omega}{\pi} \int_0^{\frac{\pi}{\omega}} A_w \omega \cos(\omega t)\, dt = \frac{2LA_w\omega}{\pi} \tag{2.4}$$

where L is the span length of the wing and A_w is the amplitude of the wing stroke.

Table 2.1 gives the scaled parameters for the robophysical system. The resulting kinematics are roughly on the order of $Re = 10^2 - 10^4$, so the observations from our experiments should be transferable to microrobotic or insect applications. The lowest amplitude-frequency combinations are on the order of small insects like flies and bees, and the highest are closer to larger insects like moths, as well as some small birds.

It should be stated: part of the challenge of dynamic scaling for this device is that typically, individual species of insects fly using a much smaller range of amplitudes and frequencies than we are exploring in this study. As a result, it is impossible to maintain a constant Reynolds number, or even a narrow range of Reynolds numbers, as would be needed to study the dynamics of a single species of insect. Instead, this study seeks to reveal features of the

parameter space that may suggest why insects operate in those regimes, and to inform future

design and control of series-elastic FWMAVs.

Table 2.1: Scaling Parameters for the Robophysical System

Parameter	Value	Units
Wing Span Length	10	cm
Mean Wing Chord Length	3.6	cm
Kinematic Viscosity of Water	8.01×10^{-7}	$\dfrac{m^2}{s}$
Amplitude Range	10 - 64	deg
Frequency Range	0.5 - 4.1	Hz
Reynolds Number Range	~200 - 14000	-

2.3 Robophysical System Design
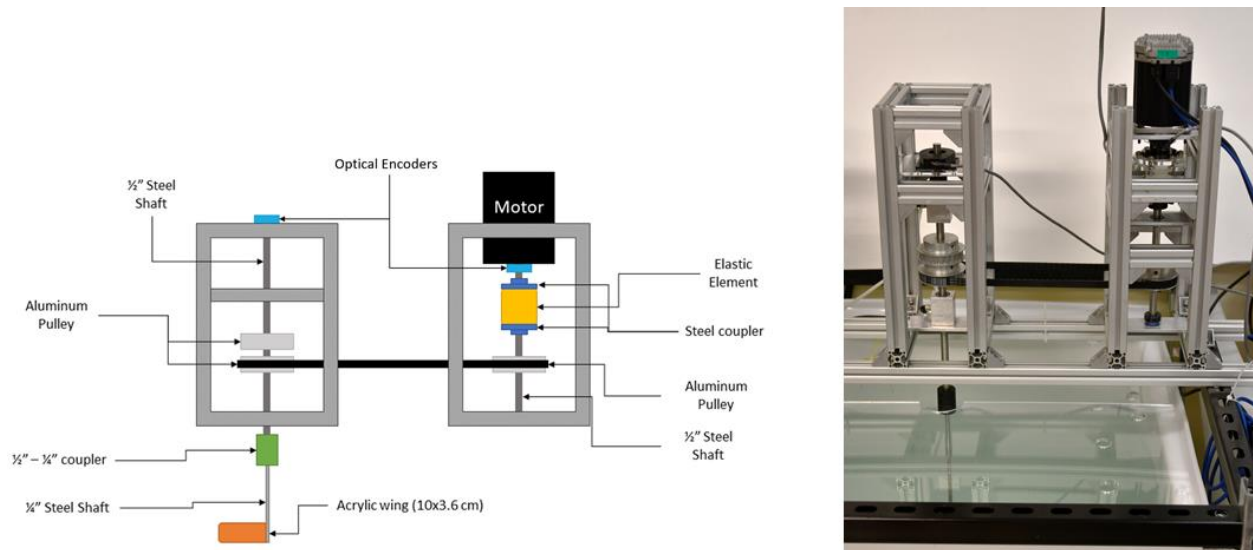
Fig 2.2: (left) Robophysical system diagram. (right) Photo of robophysical system

The series-elastic robophysical system has been designed to reflect the simplified model introduced in Section 2.1 as closely as possible. The primary frame is constructed from T-Slot aluminum and is supported above a 560 liter (147.9 gallon) plastic tank filled with water by a secondary frame of steel struts. To reduce undesirable vibrations in the secondary frame, it is constrained by nylon ratchet straps wrapped around the tank.

The primary frame houses the components that constitute the series-elastic transmission. These components include:

- A high-torque servo for direct position control

- A silicone rubber torsion spring that acts as an elastic element

- A rigid transmission consisting of aluminum pulleys, a fiberglass-reinforced neoprene L-series timing belt, lubricated ball bearings, and air bushings

- A fixed-pitch, rigid acrylic wing fixed to a rotating shaft

- Optical encoders on both the motor and wing shafts to track angular position

The following sections discuss the design and selection of these components.

2.3.1 Servo Motor Selection

We seek to use this robophysical device to better understand features of series-elastic wing dynamics that arise from changes in input trajectory, system stiffness, and system inertia. We would like to be able to decouple the motor dynamics from the system dynamics, which means that the dynamics of the motor and motor controller must be significantly faster than the desired input signal. In other words, we need a motor with position control capabilities and a high enough operating torque that the torques exerted on the system by the fluid are relatively small.

Figure 2.3: Image of Teknic ClearPath servo motor

The selected motor is a high-torque servo (Teknic ClearPath-SDSK Integrated Servo System) (Fig. 2.3). It is designed for similar applications to stepper motors, but it features higher continuous torque (3.4 Nm) and more customization options than a typical stepper motor.

The predicted maximum torque on the motor due to fluid drag is

$$T_{max} = C\dot{\theta}_w^2 \left(\frac{L}{3}\right). \tag{2.5}$$

Computing C based on [1] using the parameters defined in Table 2.1 and plugging into Equation 2.5 gives a maximum torque of

$$T_{max} = (0.0209\ Ns^2)(4.5\ Hz)^2 \left(\frac{0.1}{3}\ m\right) \approx 0.014\ Nm$$

This maximum theoretical torque is two orders of magnitude smaller than the continuous torque of the motor, so we can safely assume that the dynamics of the motor and system are decoupled.

The servo has two options for position/velocity control: step and direction or A/B quadrature. To achieve precise position control, we chose the step and direction option with a 4096 CPR resolution. We use a Pololu TIC 834 USB Multi-Interface Stepper Motor Controller

to convert continuous analog voltage signals from a USB DAQ unit to high-frequency step and direction signals. More details on the electronics and control scheme can be found in Section 2.4.

2.3.2 Series-Elastic Element

A key component of the series-elastic wing system is the elastic element itself. Early versions of the robophysical device used metal extension springs to achieve the desired effect. Aluminum timing belt pulleys were fixed to the motor and wing shafts, respectively, and an inextensible reinforced nylon timing belt was used to connect them. The springs were incorporated by cutting the timing belt and using 3D-printed adapter pieces to insert the metal springs, as shown in Figure 2.4.
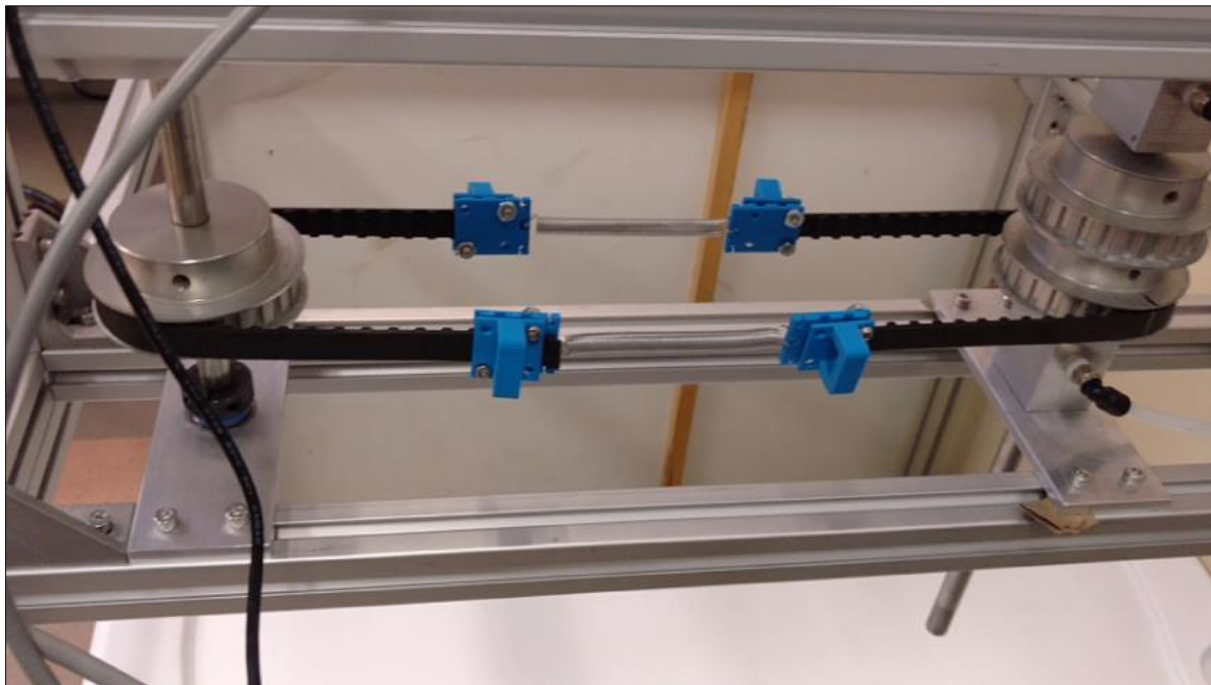
Figure 2.4: Robophysical system prototype with steel extension springs

This solution was functional and produced preliminary data, but the metal springs introduced mechanical limits on the range of the device that limited the capabilities of the system. If the amplitude of the motion of either shaft exceeded a certain limit (as may happen at resonance), the spring-belt adapters would collide with the pulley and cause the belt to fall off

and invalidate that experiment. Further, it was difficult to maintain the repeatability of experiments, as the springs would inevitably extend over time as they were often forced beyond the elastic regime. Beyond issues with the mechanical limits of the system, the steel springs would occasionally be forced into higher modes of vibration, causing lateral bending that was unmodelled and, at high amplitudes, could also cause the belt to slip off the pulleys. These mechanical and modeling limitations necessitated that another elastic element be developed.

To eliminate these limitations, a cast silicone torsion spring (Fig. 2.5) was designed to replace the steel springs. Silicone was chosen for its desirable material properties, including linear elasticity even at large strains and durability over time, and for its ability to be formed into various geometries.

2.3.2.1: Specifying the Geometry of the Silicone Element

The silicone elastic element in this robophysical system is modeled as a linearly elastic, cylindrical torsion spring whose governing equations are

$$T = \frac{\pi G r^4}{2L} \phi \tag{2.6}$$

$$\gamma = \frac{r}{L} \phi \tag{2.7}$$

Where T is the torque due to deflection ϕ, G is the shear modulus of the silicone material, γ is the maximum shear strain in the element, r is the radius of the cylinder, and L is the length of the cylinder. From these equations, we may design a spring with a specified stiffness given a known shear modulus, G. Additionally, the strain rate, $\frac{r}{L}$, is directly controllable by changing the geometry. By keeping the strain rate small, the spring remains in the linear elastic region even at larger deflections. In order to minimize the unmodeled effects of twisting at the end joints, the silicone element was designed in an "I" shape whose flanges are clamped to adapters that attach to the transmission shafts.
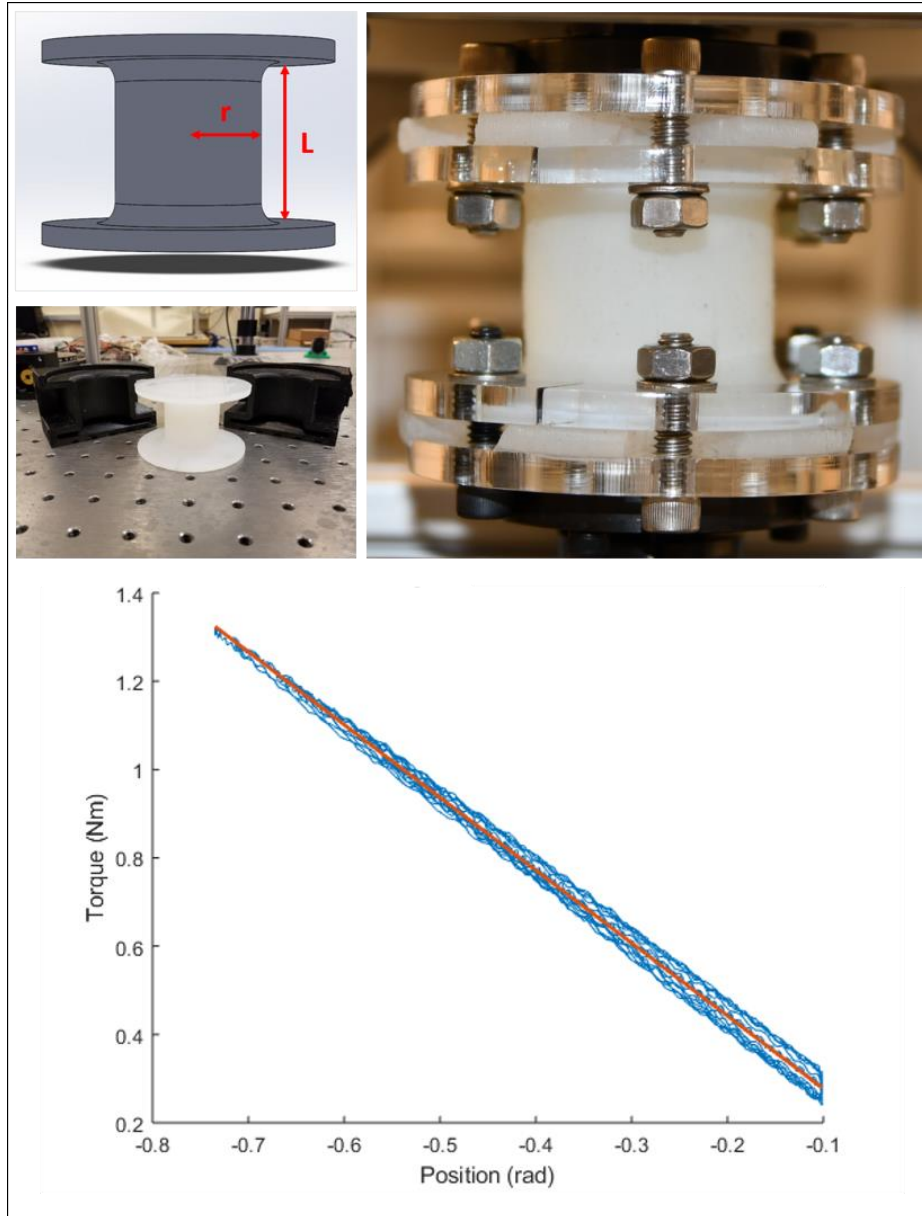
Figure 2.5: Design, fabrication, and testing of a silicone torsion spring. (Top) The geometry of the element is determined by the desired stiffness and strain rate and created in 3D CAD software. A mold with a negative geometry corresponding to the desired shape is 3D printed and Dragon Skin™ 20 platinum cure liquid silicone is prepared and poured into the mold. After 24 hours, the silicone element is removed from the mold and fixed between acrylic plates affixed with steel flange collars that act as adapters to the motor and wing assemblies. (Bottom) Results of a torsion test to characterize the elasticity of a silicone torsion element. Raw test data are shown in blue, while the least squares fit is shown in rad. Given an element with known geometry, this method was also used to determine the shear modulus of the silicone, which was not available from the manufacturer.

2.3.2.2: Silicone Element Fabrication and Properties

The process of fabricating a silicone torsion element begins by creating a mold in CAD software which is the negative of the desired geometry. The model is then 3D printed in two parts and assembled. Silicone release spray is used to prepare the surface that will come in contact with liquid silicone, and the seam between the halves of the mold is sealed using tape and a thin rubber gasket cut into the shape of the mold, if necessary, to prevent leaks.

The silicone comes in two parts, A and B, which are measured out in equal portions (by mass) so that the total volume of the mixture is the volume of the silicone element. The mixture has a pot life of 25 minutes, in which time it must be blended thoroughly and de-gassed in a vacuum chamber to minimize the occurrence of air bubbles in the final product. Finally, the two-part mixture is poured into the 3D-printed mold and allowed to cure for 24 hours before being removed and prepared for use in experiments

Several silicones – with hardnesses ranging from Shore 00-10 to Shore 30A – were tested in a custom torque measurement apparatus, and shear moduli were determined for the 10A, 20A and 30A silicones (Table 2.2). Testing confirmed that there is a linear relationship between deflection and torque for angles up to 0.8 radians (~46 degrees) and minimal hysteresis effects. The 20A silicone was selected as most able to provide the desired stiffnesses given the geometric constraints of the robophysical device, and elements of several different stiffnesses were produced (Table 2.3).

Table 2.2: Shear Moduli of Select Silicones

Name	Shore Hardness	Shear Modulus (kPa)
Dragon Skin 10 (SmoothOn)	10A	72.26
Dragon Skin 20 (SmoothOn)	20A	145.96
Dragon Skin 30 (SmoothOn)	30A	261.97

Table 2.3: Fabricated Silicone Elements

Silicone Element	Radius (cm)	Length (cm)	Stiffness (Nm/rad)
A	1.27	4.0	0.150
B	1.48	4.0	0.275
C	1.625	4.0	0.400
D	1.74	4.0	0.525

2.3.3: Rigid Transmission Components

The rigid components of the robophysical transmission were designed to transmit torque while minimizing energy loss to friction. The motor is coupled to the input end of the silicone spring by a steel flange coupler. On the output end, the same coupler is used to connect the spring to a ½" steel shaft constrained by lubricated ball bearings. An aluminum timing belt pulley (Diameter: 3.094") is fixed to the shaft and transmits torque to the primary wing shaft via a ½" L-series timing belt (fiber-reinforced nylon). The ½" shaft is constrained by a pair of air bushings, which provide superior friction reduction. A step-down coupler is then used to connect the primary wing shaft to the secondary wing shaft, a ¼" steel shaft to which the acrylic wing is affixed.

Alignment and proper lubrication of these components is crucial to the function of the robophysical system. Unmodeled friction may invalidate testing results, so care must be taken to regularly inspect the primary frame assembly, correcting misalignments, tightening bolts, applying lubrication, and maintaining proper belt tension.

2.3.4: Fixed-Pitch Acrylic Wing

Flying insects and most FWMAVs have flexible wings that rotate along the wing span due to aerodynamic loading and inertial acceleration during the wing stroke. The effect that this rotation and accompanying variation of angle of attack has on lift, drag, and power requirements

has been studied [34] and is further complicated by compliant properties of the wings themselves. In order to simplify our analysis and further focus on the dynamics of the wing transmission itself, a fixed-pitch, rigid acrylic wing (Fig. 2.5) was selected for this initial investigation. The wing is a 10 cm x 3.6 cm rectangle made of clear, ⅜" acrylic whose edges have been filed to a smooth curve. It is fixed to a ¼" steel shaft by an aluminum adapter and its pitch can be pre-set by adjusting the adapter.

2.3.5: Optical Encoders

The functionality of the robophysical system depends on reliable measurement of the angular position of the motor (input) and wing shaft (output). This is achieved using two optical rotary encoders (US Digital) – one fixed to the input side of the elastic element, and the other to the wing shaft. Each encoder disk has a resolution of 1024 CPR, which results in a functional resolution of 4096 CPR via quadrature. Output from the encoders is collected continuously during operation and analyzed during post-processing in Matlab.

2.4: Experiment Design & Data Collection

This robophysical model of a series-elastic wing enables us to investigate how the series-compliance of a flapping wing transmission influences the dynamics and control of flapping wing systems. To do this, we ran a series of steady-state experiments varying

- Motor input amplitude and frequency (Table 2.1),
- Silicone spring stiffness (Table 2.3), and
- Total system inertia (Table 2.4).

The system inertia was varied by fixing a circular aluminum plate (Figure 2.6) to the wing shaft and adding mass in the form of steel nuts, and the spring stiffness was varied by swapping out different silicone springs for each suite of tests. The acrylic wing was fixed at a 90-

degree angle of attack for all tests, maximizing drag and increasing the likelihood of significant

wing-wake interactions [1].
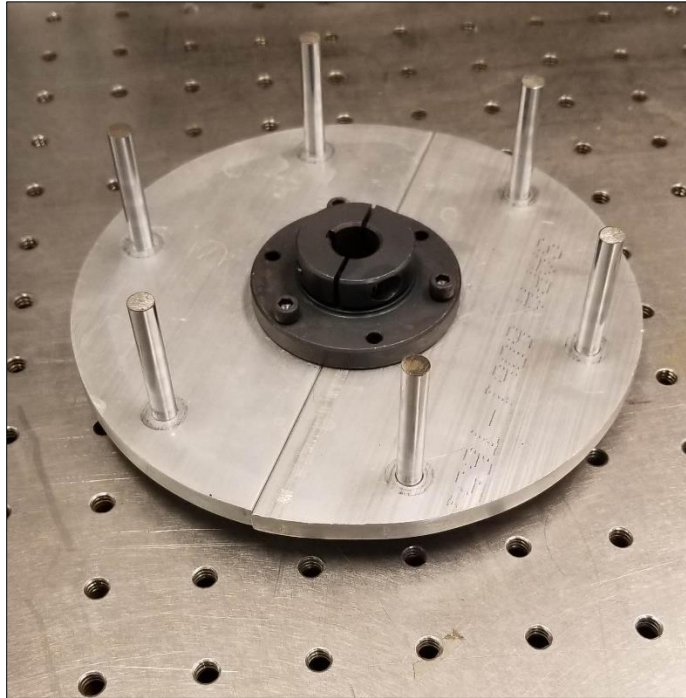
Fig 2.6: Photo of inertia plate used to vary inertia for experiments

Table 2.4: System Inertia Values for Amplitude-Frequency Sweep Tests

Name	I_1	I_2	I_3
Inertia (kg m^2)	0.00136	0.00259	0.00290

Figure 2.7 provides a diagram of the experiment process. In Matlab, the user prescribes

two vectors of amplitudes and frequencies at which to run tests. The code runs through each

combination, generating a reference signal and queueing it for output to a NI USB DAQ. When

the DAQ is triggered, it outputs an analog voltage between 0 and 5V to a TIC834 stepper driver

that converts the signal into step and direction commands that allow the motor to follow the

reference signal as a displacement target. For 30 seconds the motor drives the series-elastic wing

while the motor and wing encoder channels are sampled at 1kHz and the instantaneous counts

and run time are saved in a text file. Once all of the combinations of parameters have been

exhausted, the next spring and inertia are installed and experiments are repeated.
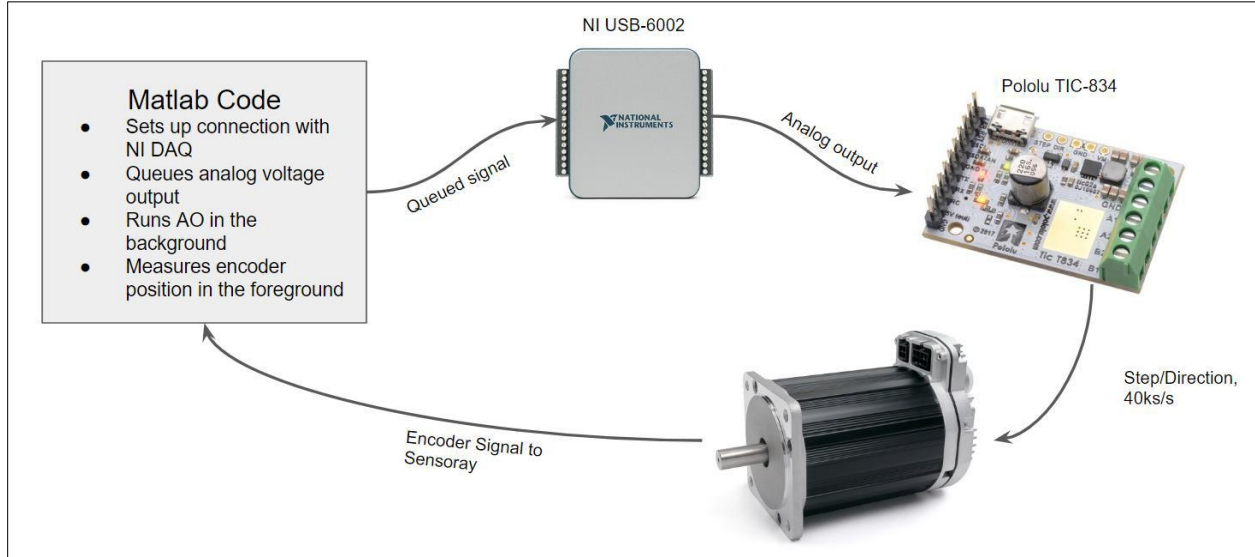
Figure 2.7: System operation process diagram. For each combination of amplitude and frequency
tested, the Matlab generates a stroke profile and queues it for the NI USB DAQ. It then triggers the NI
DAQ output to send an analog voltage to a stepper motor controller, which translates the signal into an
angular reference position relative to the starting point. It sends step and direction signals to the servo to
follow the reference position, causing the servo to move based on the analog signal. During operation,
motor and wing encoder positions are tracked in dedicated channels on a Sensoray 826 PCI board. The
encoder channels are polled at 1kHz and stored in text files.

2.5: Data Processing

Once a full suite of tests has been run, the data collected is processed in Matlab. The

encoder readings are loaded from text files and trimmed to remove transient start-up and end

effects. Since both signals are very nearly sinusoidal, we perform an FFT on each, obtaining the

amplitude, frequency, and phase of the principal component of the signal, though we use only the

amplitude. We define the amplitudes as shown in Figure 2.8, and define an *amplitude gain*:

$$Gain = \frac{A_{wing}}{A_{mot}}$$

Amplitude gain is the primary metric we use for our analysis. Its significance is discussed in

detail in Chapter 3.
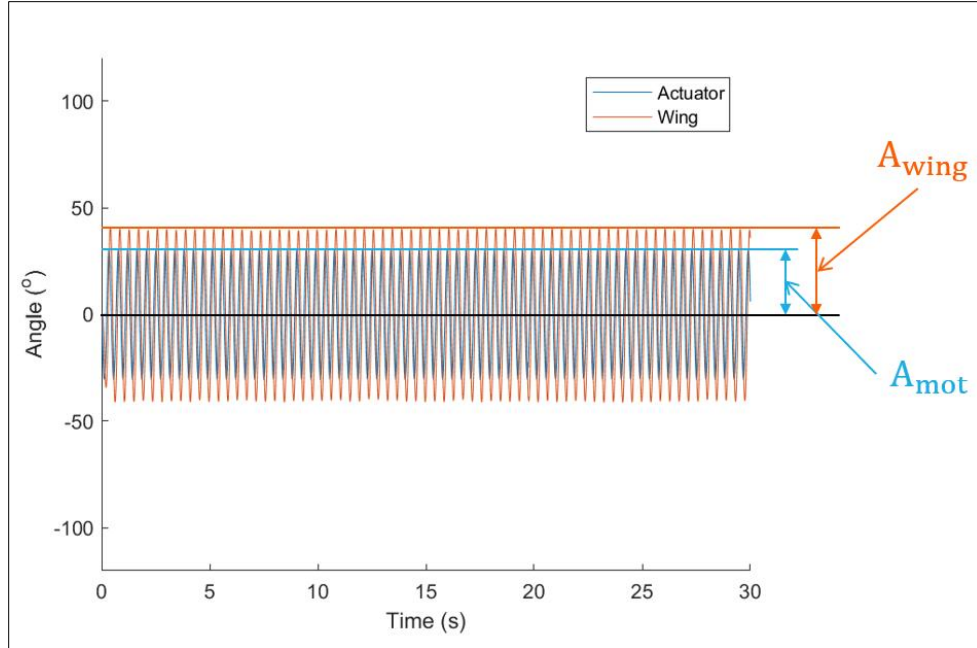
Figure 2.8: Representative example of raw data before processing. The encoder position of the wing and motor are tracked by the Matlab code. The amplitudes of oscillation, A_{mot} and A_{wing}, respectively, are computed via FFT, along with frequencies and phase delays.

CHAPTER 3: RESULTS & DISCUSSION

A suite of tests was performed to investigate the resonance properties of a series-elastic flapping wing system. The actuation amplitude was varied across 19 values from 10 to 64 degrees and the frequency across 19 values from 0.5 to 4.1 Hz. For each combination, the amplitude gain was computed as defined in Chapter 2.5. A plot showing the gains from a single input amplitude is shown in Figure 3.1B, and a heat map of gains over amplitude and frequency is presented in Figure 3.1C.

3.1: Amplitude-Frequency Sweep Results
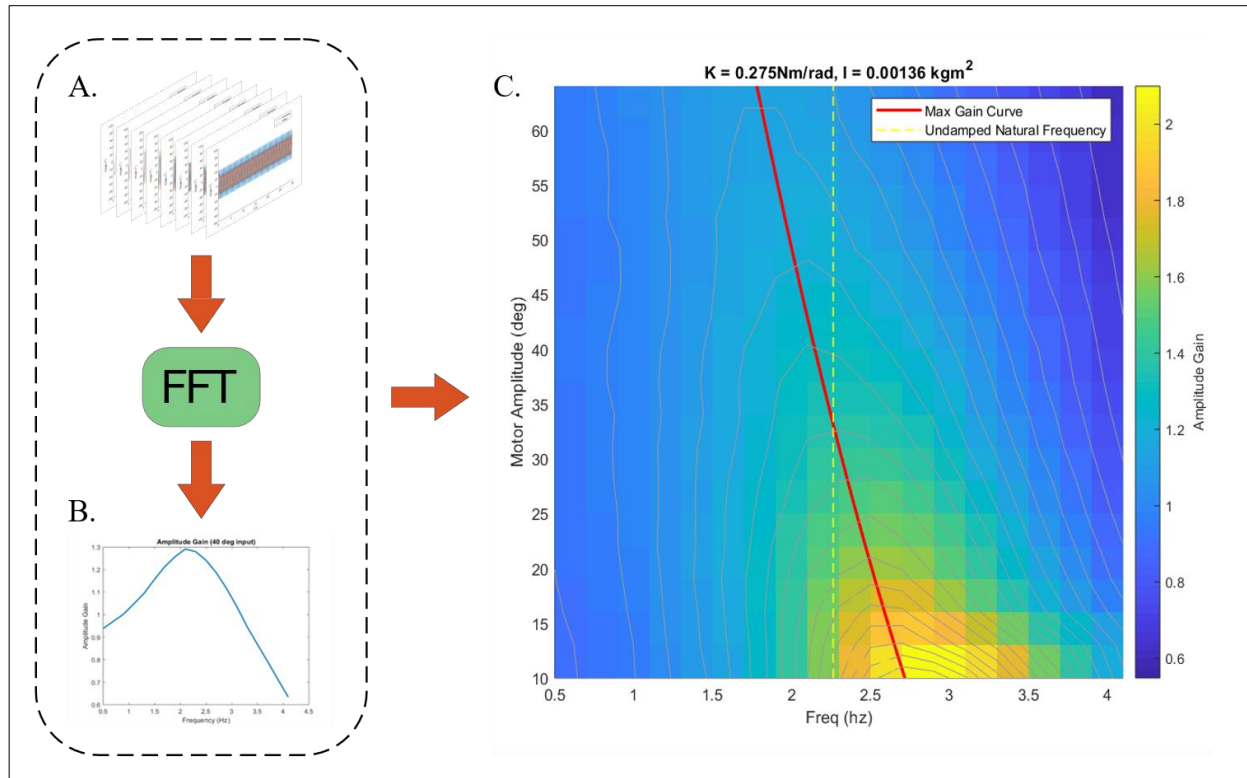
Figure 3.1: Construction of amplitude gain maps. (A) For each input amplitude, 19 tests were run across frequencies between 0.5 and 4.1 Hz and stored. (B) The amplitudes of the wing and motor trajectory, respectively, were found using FFT in Matlab and divided to generate the amplitude gain for that trial. (C) The process was repeated over each motor input amplitude (19 tests between 10 and 64 deg), and the gains were plotted as a heat map whose color corresponds to amplitude gain. The resonant peaks were computed for each input amplitude, and a line (shown in red) was fit to smoothly indicate the peaks. For comparison, the undamped natural frequency for the specified stiffness K and inertia I.

In order to observe the effects on gain of changes in spring stiffness and total system inertia, further suites of tests were performed across 4 silicones with varying stiffnesses (See Table 2.3) and 3 values of system inertia. The system inertia was varied by the addition of an aluminum plate and steel nuts to the wing shaft. Added mass was calculated roughly as a cylinder of water with a height equal to the span length of the wing and a diameter equal to its chord length

Figure 3.2 shows the gain maps resulting from each combination of stiffness and inertia tested. Figure 3.3 represents the same data but rotated about the frequency axis and weighted by the input amplitudes to visualize the wing amplitude for various configurations. The following section will discuss some of the relevant features of this data.

3.2: Features of Gain Plots

The amplitude gain plots in Figures 3.2 and 3.3 represent a sample of the series-elastic flapping wing parameter space that enables us to describe some of the general behavior of these complex systems.

3.2.1: Resonance Behavior

As expected, the series-elastic flapping wing system exhibits resonance. Gains are near unity at low frequencies where the influence of fluid drag forces are small relative to the stiffness of the spring. Gain reaches its peak at a resonant frequency, after which it drops off. At those higher frequencies where gain is less than unity, the spring actually *limits* the performance of the wing. Unlike the familiar harmonic oscillator, however, the resonant frequency is a function of amplitude
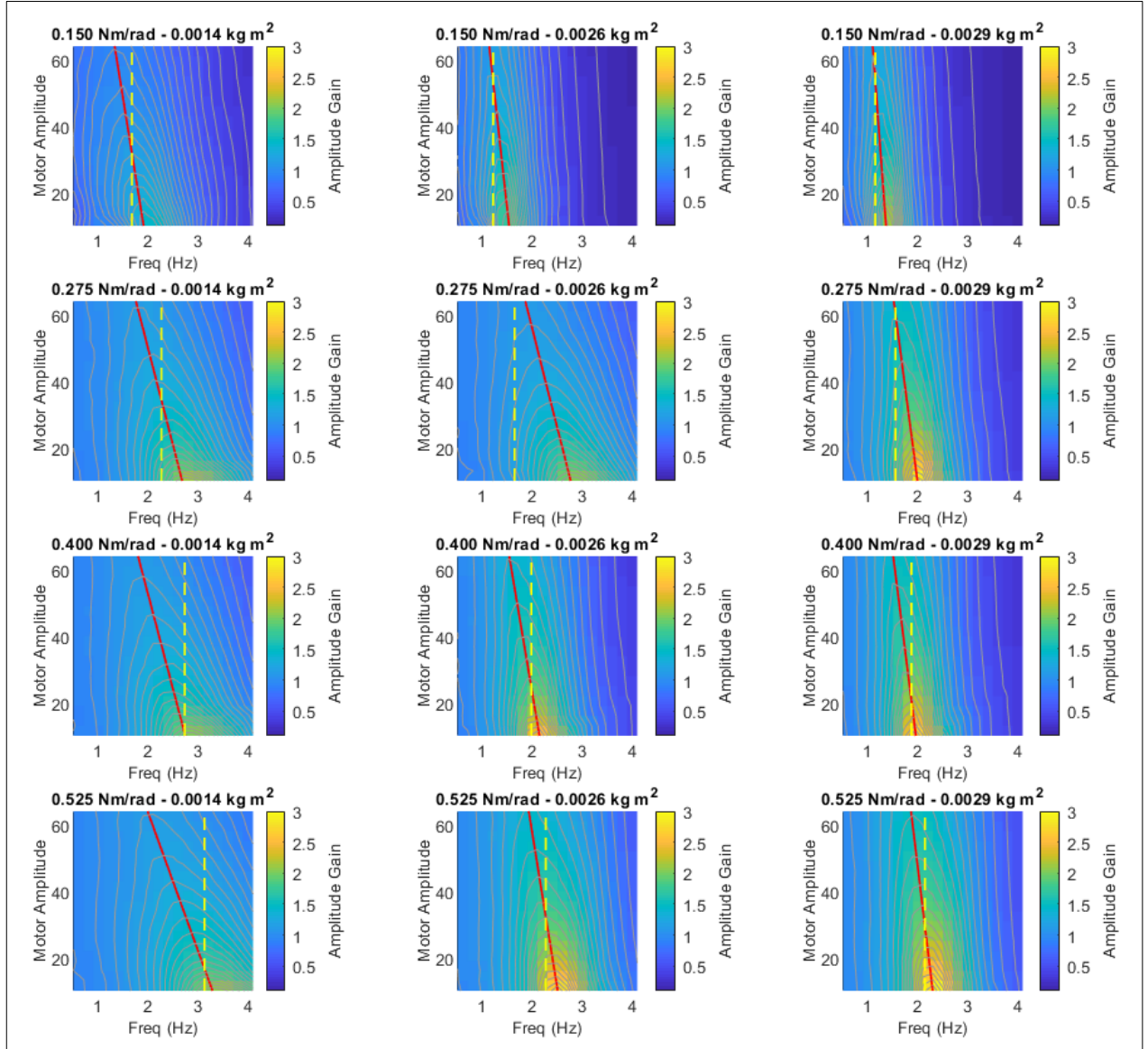
Figure 3.2: Amplitude gain heatmaps for varying stiffness and inertia. Each plot above represents a suite of experiments with varying motor amplitudes (vertical axis) and frequencies (horizontal axis). Silicone spring stiffness increases top-to-bottom, and inertia increases left-to-right. The color corresponds to the gain at each test configuration ranging from 0.1 (blue) to 2.9 (yellow). Amplitude gain is highest at low amplitudes for all configurations, but peak gains are generally higher for higher inertia. However, higher peaks come with steeper drop-off when the frequency is away from resonance; in contrast, gain is close to unity across a wide range of frequencies for lower inertia configurations. The peak gain for each input amplitude is fit to a line (red), and the undamped natural frequency computed from the stiffness and inertia is provided for reference (yellow dashed). In configurations where the inertia is smaller, the peak gain has a relatively strong dependence on motor amplitude, whereas the dependence is much smaller for high-inertia cases.
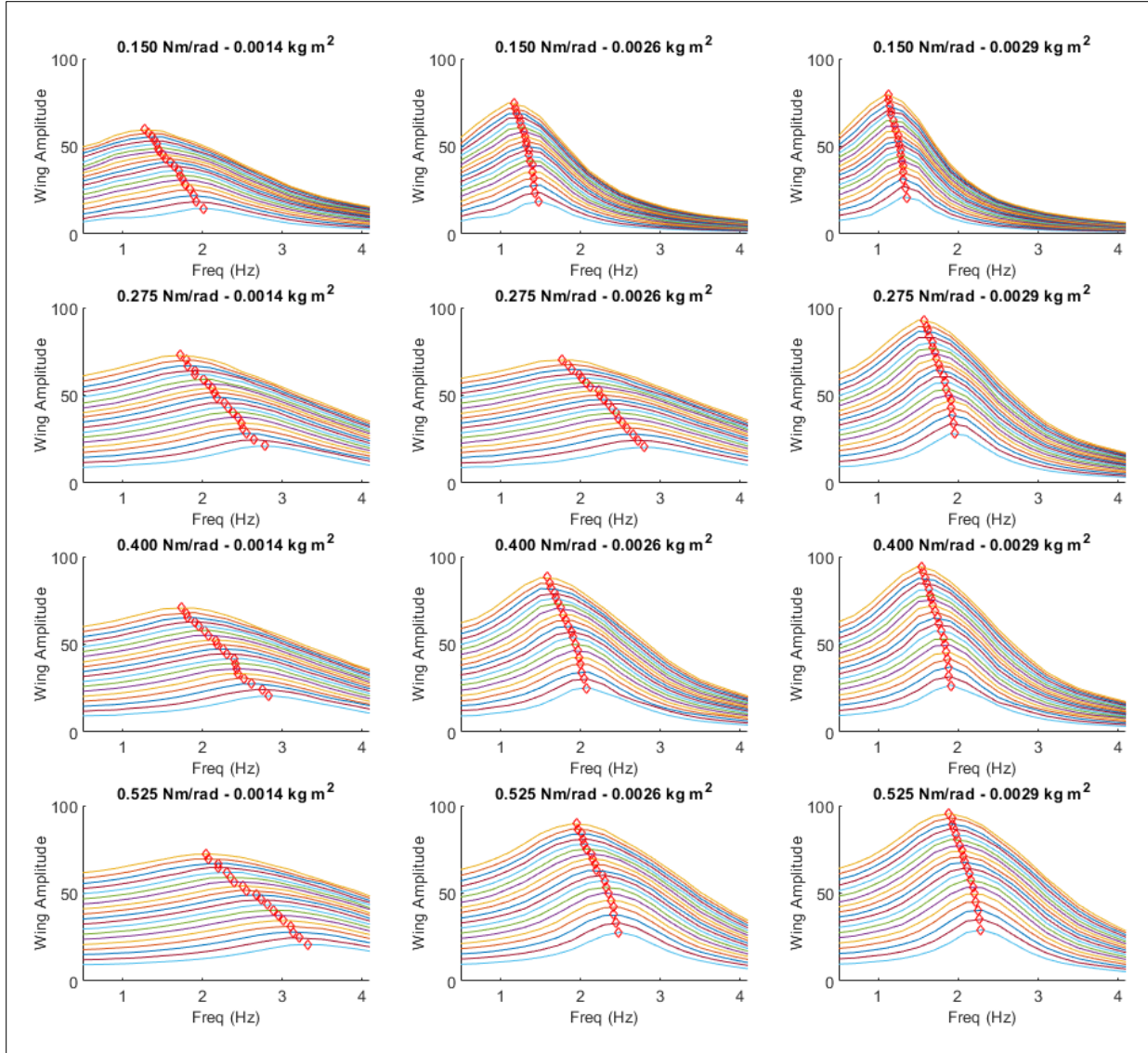
Figure 3.3: Wing amplitudes resulting from varying input parameters. These plots represent the same data as in Fig. 3.2 but rotated about the frequency axis and weighted by the motor amplitude. Each line in a plot represents the wing amplitudes resulting from a single motor amplitude across frequencies; the lowest motor amplitudes are at the bottom, and the highest are at the top. The peak output amplitude corresponding to maximum gain is marked by a red diamond. Note that the amplitude bandwidth (the difference between the highest and lowest wing amplitude over all motor amplitudes) is severely attenuated at high frequencies when the ratio of stiffness to inertia $\frac{K}{I}$ is small. When $\frac{K}{I}$ is larger, however, the bandwidth remains relatively consistent over frequencies.

3.2.2 Resonance Frequency Dependence on Motor Amplitude

It is clear by looking at Figures 3.2 and 3.3 that the measured resonance frequency is a

function of amplitude, especially for configurations where stiffness is high and inertia is low, i.e.

the quantity $\frac{K}{I}$ is large. This effect appears to be due to the linear relationship between amplitude

and maximum wing velocity ($u_{max} = A_w\omega$) combined with the quadratic relationship between

fluid damping and velocity. The higher the amplitude, the larger the influence of fluid drag,

which shifts the resonant peak lower.

However, this effect is diminished when I is large compared to K, i.e. $\frac{K}{I}$ is small. When the

inertia increases, the force required to accelerate the wing increases, and the relative influence of

drag on the wing system is decreased. In the case of an oscillator with linear damping, the

damped natural frequency can be found to be

$$\omega_d = \sqrt{\frac{k}{I} - \left(\frac{c}{2I}\right)^2}$$

When I is large, ω_d approaches the undamped natural frequency: $\omega_n = \sqrt{\frac{k}{I}}$. Similarly, the

systems with highest inertia and lowest spring coefficient behave as if they are subject to less

damping than other configurations.

3.2.3 Wing Amplitude Bandwidth Varies with System Parameters

Another feature of the series-elastic system can be observed from the wing amplitude

plots in Figure 3.3; when the stiffness of the transmission is held constant, increases in inertia

result in more severe attenuation of the wing amplitude bandwidth at high frequencies. At

frequencies below resonance where gains are near unity, there is a broad range of wing

amplitudes that are reachable by actuating the system at some amplitude. Above resonance, gains

that are less than unity start to reduce the range of possible wing amplitudes. This effect is most

severe for systems with high inertia.

This bandwidth attenuation effect is important for designers of series-elastic flapping wing systems because it represents a kind of *saturation* that could limit the control authority they may exert on the system. A potential flying robot may choose to have a high wing and transmission inertia to take advantage of the large peak gains observed in Figure 3.2, but it would be forced to operate within a small range of frequencies to maintain controllability. This result could also suggest a reason why insects may remain within a small range of frequencies: not only is it favorable for efficiency, it may also be important for consistent flight control.

3.3: Aerodynamic Power and Amplitude Gain

The amplitude gain displayed in the plots in Section 3.1 is a metric that is clearly important to the performance of such series-elastic systems; larger gain means larger output amplitude, which means that the actuator will do less work to achieve the same output dynamics. However, it is necessary to explicitly demonstrate this relationship.

As a first step, we derive expressions for the input and output power for the system. The equation of motion of the forced series-elastic wing is

$$I\ddot{\theta}_w = k(\theta_m - \theta_w) - F_{aero} \tag{3.1}$$

Using the simplified model presented in Chapter 2, Equation 3.1 becomes

$$I\ddot{\theta}_w = k(\theta_m - \theta_w) - \bar{C}\dot{\theta}_w^2 \tag{3.2}$$

Where I is the inertia of the system, k is the torsional stiffness of the silicone spring, $\bar{C}$ is the mean coefficient of aerodynamic drag on the wing, and θ_m and θ_w are the angular position of the motor and wing, respectively. The instantaneous energy of the system can be given as the sum of two components: the inertial (kinetic) energy, E_I, and the spring (potential) energy, E_S. There is also energy lost to fluid drag, E_D, defined over a single cycle:

$$E_I = \frac{1}{2}I\dot{\theta}_w{}^2 \tag{3.3}$$

$$E_S = \frac{1}{2}k(\theta_m - \theta_w)^2 \tag{3.4}$$

$$E_D = \int_0^{\frac{1}{\omega}} C_D \dot{\theta}_o^3 \, dt \tag{3.5}$$

where ω is the driving frequency from the motor. By conservation of energy:

$$W_{in} - E_I - E_S - E_D = 0 \tag{3.6}$$

Taking the derivative of (3.6):

$$
\begin{aligned}
P_{in} &= \dot{E}_I + \dot{E}_S + \dot{E}_D \\
&= I\dot{\theta}_w \ddot{\theta}_w + k(\theta_m - \theta_w)(\dot{\theta}_m - \dot{\theta}_w) + \bar{C}\dot{\theta}_w^3
\end{aligned} \tag{3.7}
$$

Combining (3.2) and (3.7), we get an expression for the power input:

$$
\begin{aligned}
P_{in} &= m\dot{\theta}_w \ddot{\theta}_w + k(\theta_m - \theta_w)(\dot{\theta}_m - \dot{\theta}_w) + \bar{C}\dot{\theta}_w^3 \\
&= \big(k(\theta_m - \theta_w) - \bar{C}\dot{\theta}_w^2\big)\dot{\theta}_w + k(\theta_m - \theta_w)(\dot{\theta}_m - \dot{\theta}_w) + \bar{C}\dot{\theta}_w^3 \\
&= k(\theta_m - \theta_w)\dot{\theta}_w + k(\theta_m - \theta_w)(\dot{\theta}_m - \dot{\theta}_w) \\
&= k(\theta_m - \theta_w)\dot{\theta}_m = F_{spring}\dot{\theta}_m
\end{aligned} \tag{3.8}
$$

Equation 3.8 allows us to compute the motor power input from only the kinematics of the actuator and wing given that we know the stiffness of the silicone element. The useful power output of the wing is given by

$$
\begin{aligned}
P_{out} &= \dot{E}_I + \dot{E}_D \\
&= I\dot{\theta}_w \ddot{\theta}_w + \bar{C}\dot{\theta}_w^3
\end{aligned} \tag{3.9}
$$

Substituting (3.2) into (3.9):

$$
\begin{aligned}
P_{out} &= \big(k(\theta_m - \theta_w) - \bar{C}\dot{\theta}_w^2\big)\dot{\theta}_w + \bar{C}\dot{\theta}_w^3 \\
&= k(\theta_m - \theta_w)\dot{\theta}_w = F_{spring}\dot{\theta}_w
\end{aligned} \tag{3.10}
$$

We are interested in examining how series-elastic transmissions affect the power requirements of flapping wings, so we may propose a *power ratio, R_P,* defined as the ratio between the output and input power:

$$R_P = \frac{P_{out}}{P_{in}} \tag{3.11}$$

Plugging (3.8) and (3.10) into (3.11) yields

$$R_P = \frac{k(\theta_m - \theta_w)\dot{\theta}_w}{k(\theta_m - \theta_w)\dot{\theta}_m} = \frac{\dot{\theta}_w}{\dot{\theta}_m}, \tag{3.11}$$

revealing that the ratio of output and input power is equivalent to the ratio between the velocities of the motor and wing. The input θ_m is prescribed as sinusoidal and we assume that θ_w is close to sinusoidal with the same frequency and phase delay ϕ,

$$\theta_m(t) = A_m \sin(\omega t) \tag{3.12}$$

$$\theta_w(t) = A_w \sin(\omega t + \phi) \tag{3.13}$$

Taking derivatives of (3.12) and (3.13) and plugging into (3.11),

$$R_P = \frac{A_w \omega \cos(\omega t + \phi)}{A_m \omega \cos(\omega t)} \tag{3.14}$$

Taking the average over one cycle,

$$R_P = \frac{A_w}{A_m} = Gain \tag{3.15}$$

Which is equivalent to the amplitude gain computed from our experimental data. Therefore, the observed amplitude gain of the series-elastic system is a measure of the ratio of the cycle-averaged output power to the cycle-averaged input power.

3.4: Maximum Gain and Optimal Stiffness

Now that we have an expression for gain that is informed by the dynamics of the system, we may describe the conditions at which the amplitude gain will be maximum. Combining the definition of amplitude gain with Equations (3.11), (3.7), and (3.9),

$$Gain = R_P = \frac{\bar{P}_{out}}{\bar{P}_{in}} = \frac{\overline{\dot{E}_I + \dot{E}_D}}{\overline{\dot{E}_I + \dot{E}_S + \dot{E}_D}} = \frac{k(\theta_m - \theta_w)\dot{\theta}_w}{k(\theta_m - \theta_w)\dot{\theta}_m} \tag{3.16}$$

with bars to indicate that the terms are averaged over a cycle. In the case when stiffness k is very large (a rigid transmission), $\dot{E}_S$ approaches zero, and the amplitude gain is unity. The wing trajectory tracks the actuator input exactly and the power input is equal to the power output. However, when k is small relative to the inertial and aerodynamic loadings, $\dot{E}_S$ becomes a function of the motor input and the inertia, stiffness, and aerodynamic parameters, and, by extension, so does the amplitude gain.

If we define a desired wing trajectory, P_{out} is constant for a system with a certain inertia and aerodynamic drag coefficient, and gain is maximized by choosing a stiffness that minimizes P_{in}. In order to identify this optimal stiffness, we follow a similar process to Bennett et al. [15], investigated a comparable problem in the flukes of cetaceans. They derive an expression for a dimensionless input power, $\hat{P} = \frac{P_{in}}{IA_w^2\omega^3}$:

$$\hat{P} = \cos \omega t \left(\hat{C}\cos^2 \omega t - \sin \omega t\right)\left[1 - \hat{K}^{-1}\left(2\hat{C}\sin \omega t + 1\right)\right] \tag{3.17}$$

where $\hat{C} = \frac{\bar{C}A_w}{I}$ is a dimensionless number that represents the ratio of peak hydrodynamic force to peak inertial force and $\hat{K} = \frac{k}{I\omega^2}$ is the dimensionless ratio of the strain energy at the end of the stroke to the maximum kinetic energy. A graph of this parameter for different values of $\hat{K}$ is shown in Figure 3.4.

From this dimensionless power expression, it can be observed that in the case of a rigid transmission ($\hat{K} \gg 0$), the motor must do positive work to accelerate the system and overcome fluid forces and negative work to decelerate at the end of the stroke. As the stiffness decreases, some of the work of accelerating and decelerating the system may be taken up by the spring.
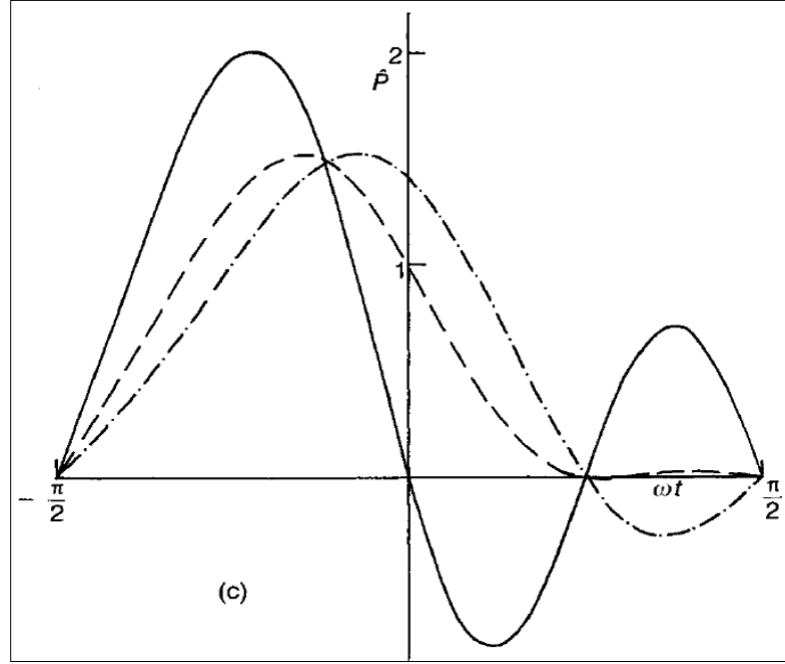

Figure 3.4: Graph of $\hat{P}$ for different values of $\hat{K}$. $\hat{P}$ is plotted over one period for three different values of the nondimensional parameter $\hat{K}$ with $\hat{C} = 1.4$. In the case of a very large $\hat{K}$ (dash-dot), the transmission is rigid and the motor must do negative work at the end of the stroke to begin reversal. In the case of a much smaller $\hat{K}$ (solid line), the strain energy in the spring is stored and released too rapidly and requires the motor to do *additional* positive and negative work to maintain the trajectory. Finally, in the optimum case, $\hat{K} = \hat{K}_{opt}$, (dashed line), the motor power is minimized over the stroke and always positive. From [14]

However, when the stiffness becomes small ($\hat{K} \leq \hat{K}_{opt}$), the strain energy in the spring is released too quickly and the motor must actually do additional work to maintain the desired wing trajectory. Therefore, there exists an optimal stiffness, which Bennett derives:

$$\hat{K}_{opt} = \sqrt{1 + 4\hat{C}^2} \tag{3.18}$$

When the dimensionless terms are expanded, the optimal stiffness for a specified wing amplitude, A_w; frequency, ω; system inertia, I; and mean coefficient of drag, $\bar{C}$ can be found via the expression:

$$k_{opt} = I\omega^2 \sqrt{1 + 4A_w^2 \frac{\bar{C}^2}{I^2}} \tag{3.19}$$

A system with this stiffness is optimal in the sense that when it is actuated at frequency ω and a motor amplitude that induces a wing trajectory with an amplitude of A_w, the power input will be minimized and the power ratio R_P will be maximized. Therefore, since R_P and amplitude gain are equivalent metrics, we should be able to use Equation 3.19 to predict the locations of the resonant peaks in the gain maps in Figures 3.2 and 3.3.

3.5: Fitting the Optimal Stiffness Curve to Experiment Data

If the optimal stiffness analysis above is sufficient to describe the resonant behavior observed in the series-elastic flapping wing system, a curve defined by rearranging (3.19):

$$\omega_{res} = \sqrt{\frac{k}{I \sqrt{1 + 4A_w^2 \frac{\bar{C}^2}{I^2}}}} \tag{3.20}$$

should predict the resonant frequency at each output amplitude and closely follow the peak wing amplitude curves pictured in Fig 3.3. Using a method from Dickinson [1] to estimate the aerodynamic drag force coefficient for the rigid wing, we find $\bar{C} \approx 0.0209\ Nms^2$. We define a curve based on (3.20) in Figure 3.5, but it severely underestimates the resonant frequency. Since the underestimation is consistent across parameters, it seems likely that the estimate of coefficient of drag is incorrect. We seek to find another method of estimating the mean coefficient of drag.

To that end, the optimal stiffness relationship may be rearranged to compute the coefficient of drag that results in resonance at a certain configuration:

$$\bar{C} = \sqrt{\frac{\left(\frac{k}{\omega^2}\right)^2 - I^2}{4A_w^2}} \tag{3.21}$$

If (3.21) is rearranged as a cost function:

$$\sqrt{\frac{\left(\frac{k}{\omega^2}\right)^2 - I^2}{4A_w^2}} - C = \gamma$$
$$\bar{C} = \min_{C} \|\gamma\| \tag{3.22}$$

minimizing γ over C will find an estimate of $\bar{C}$ that minimizes the error in the resonant frequency estimate across all configurations and amplitudes. Performing this minimization results in an estimate of $\bar{C} \approx 8.9\mathrm{x}10^{-4}\ Nms^2$. The curve corresponding to this estimate of drag coefficient is also shown in Figure 3.5. The magnitude of the estimation error over amplitudes is presented in Figure 3.6.

3.6: Does the Optimal Stiffness Curve Describe the Locations of Resonant Peaks?

This project set out to determine if a low-order analytical model like that described in Section 2.1 would be sufficient to predict the resonant behavior of a series-elastic flapping wing. In order to answer that question, we compared experimental results to results of the analysis of a simple low-order model of the system.

3.6.1: The Curve Fit to the Data Improves with Amplitude

After numerically finding an optimal coefficient of drag to fit across all test configurations and comparing the resulting curves to the experimentally determined peaks, we see that that there is still some significant error in the estimate of resonant frequency (Fig. 3.6). However, that error appears to be significantly smaller at higher amplitudes. With the exception

of the set of tests using the $0.275\ Nm\ rad^{-1}$ silicone spring (which appears to be an outlier and may be due to experiment error), the percent error in frequency estimate less than 10% for all wing amplitudes greater than 60 degrees. On the other hand, configurations with peak amplitudes *below* 60 degrees see prediction errors that are much higher, reaching 50% at amplitudes of 20-30 degrees.

It appears that there are (at least) two regimes at work here: one where our simplified model seems to more closely predict resonant frequency, and one where the observed behavior
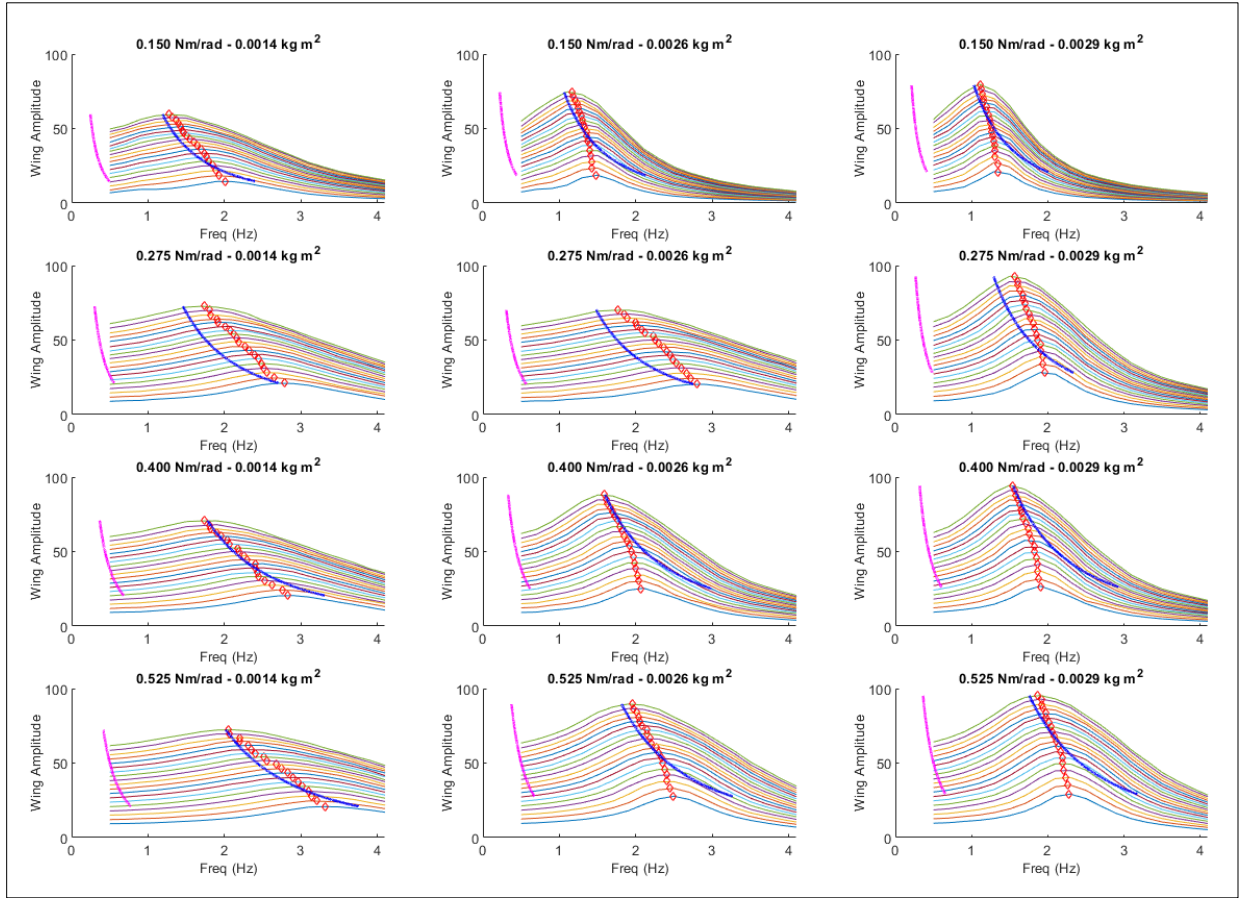
Figure 3.5: Optimal stiffness curve fitting over wing amplitude data. Two curves generated based on Equation 3.20 with different values of $\bar{C}$. The magenta curve was computed based on a geometrically determined estimate of the drag coefficient (0.0209 Nms^2) and significantly underestimates the resonant frequency of the system. The blue curve uses a value of $\bar{C}$ that was computed numerically by minimizing the error function defined in Equation 3.22.

diverges and some other unmodeled effects take precedence. To explain what might be the cause, we will first return to the optimal stiffness analysis.

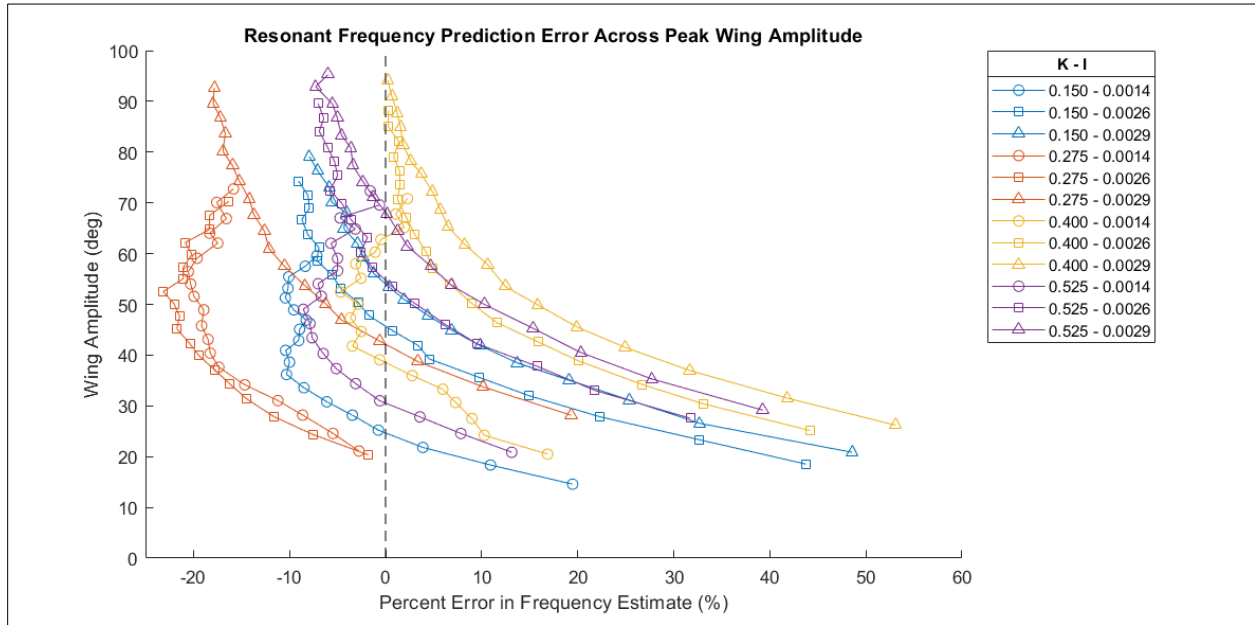**Figure 3.6: Resonant frequency prediction error across peak wing amplitude.** The plot above shows the error in resonant frequency estimate (horizontal axis) for each peak output amplitude from the plot in Figure 3.5 (vertical axis). Tests with different stiffness are displayed with different colors, and different inertias are shown using different marker shapes. Estimation error appears generally lower at high amplitudes than at low, where the error increases from ~10% to >50%.

3.6.2: Optimal Stiffness Analysis Assumptions

The analysis performed in [15] and described above depends on several important assumptions. First, it requires that the coefficient of drag force on the wing is either constant or has minimal variation from the mean over a wing stroke and thus the forces on the wing are dominated by fluid loading that has a quadratic relationship to wing velocity. It also assumes minimal variation in the inertia and spring stiffness of the system. Finally, the analysis requires that the wing trajectory is sinusoidal with the same frequency as the motor input but possibly with a different amplitude.

These assumptions may make the problem analytically tractable, but how reasonable they are is up for debate. As discussed in Chapter 1, there are several unsteady mechanisms that

contribute to the aerodynamic loading on a flapping wing in a fluid – added mass, delayed stall, wing-wake-interaction, etc. For our simplified model to be sufficient, the effects of the unsteady factors must be small compared to the quasi-steady fluid loading. Perhaps there are conditions at low amplitudes that cause the unsteady mechanisms to dominate and therefore invalidate some of the assumptions made in the optimal stiffness analysis

3.6.3: A Tale of Two Flow Regimes

Consider a wing with a 90-degree angle-of-attack moving through a fluid. Figure 3.8 depicts its trajectory and the forces it experiences during a full wing stroke, as measured by Sane and Dickinson [33]. The figure compares the drag force predicted by a quasi-steady model using a measured mean coefficient of drag to the actual force measured on their robophysical flapping wing system. The quasi steady model is proportional to the wing velocity squared, so the curve of the dotted line is smooth, nearly constant for most of the wing stroke, and always positive. The measured drag, on the other hand, features significant peaks in force at the beginning of each semi-stroke, as well as negative peaks near reversal. During those peaks, the added mass, vortex formation, and other unsteady mechanisms discussed in Chapter 1 are most significant and seem to dominate the loading on the wing. During the time that the wing is accelerating and wing vortices are forming, the simplified quasi-steady model underestimates the magnitude of forces on the wing.

The analysis performed by Bennet et al. considers only forces due to quasi-steady fluid loading. Based on the observation in Fig. 3.7, that means that it will typically underestimate the forces on the wing. However, the degree to which the quasi-steady assumption underestimates fluid forces depends on how long the wing remains in the intermediate "translation" regime

where the model fits the measured drag more closely. Consider two regimes whose durations sum to half of the wing stroke period:

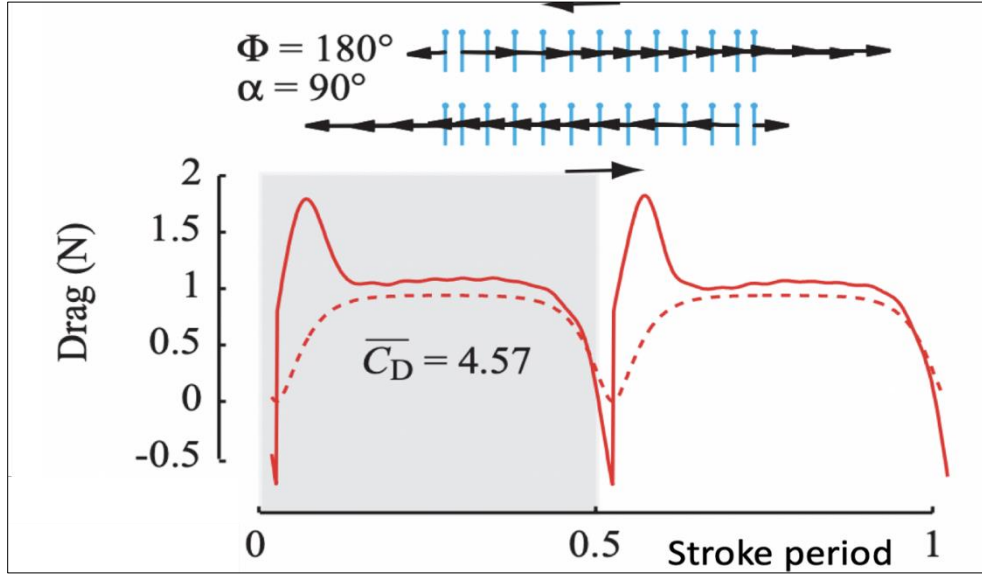$$2T_{form} + T_{trans} = \frac{1}{2\omega} \tag{3.23}$$

Figure 3.7: Wing stroke with formation and translation regimes. Measurement of drag forces on a rigid wing with a peak-to-peak amplitude of 180 degrees and angle-of-attack of 90 degrees (perpendicular to the flow) from [33]. The solid line depicts the drag force measured by load cells at the base of the wing, and the dotted line is the drag force predicted by a quasi-steady model. The quasi-steady model of drag underestimates the force, especially in the vortex formation regimes at startup and reversal. However, the quasi-steady estimate is much closer in the translation regime once the unsteady effects have dissipated.

The first constant, T_{form}, represents the time the wing spends in the unsteady regime at the beginning and ending of the stroke. It depends on the rate of vortex formation on the wing as well as terms related to added mass and wing-wake interaction. The second, T_{trans}, is the amount of time the wing spends in the "translation" regime. We define a *wing stroke ratio*:

$$WSR = \frac{T_{trans}}{T_{form}} \tag{3.24}$$

We can approximate T_{form} by using an estimate for vortex formation time from Dabiri [37]:

$$T_{form} \propto \frac{D\hat{T}}{U} \approx \frac{D\hat{T}}{A_w\omega} \tag{3.25}$$

Where D is a characteristic length, $\hat{T}$ is a dimensionless vortex formation constant, and $A_w\omega$ is the maximum velocity of a wing with amplitude A_w and frequency ω. Combining (3.23), (3.24), and (3.25) gives an expression for wing stroke ratio in terms of wing stroke profile:

$$WSR = \frac{T_{trans}}{T_{form}} = \frac{\frac{1}{2\omega} - T_{form}}{T_{form}} = \frac{1}{2\omega T_{form}} - 1 \propto \frac{A_w}{2D\hat{T}} - 1 \tag{3.26}$$

3.6.4: Wing Stroke Ratio

The definition of wing stroke ratio in Equation 3.26 suggests that the ratio of the amount of time that a wing spends in a translation regime increases with wing amplitude. This means that the quasi-steady approximation for the forces on the wing over a stroke improves with larger amplitudes, and a quasi-steady model may be better able to predict the resulting dynamics. On the other hand, as amplitude decreases, the translation regime shrinks relative to the unsteady
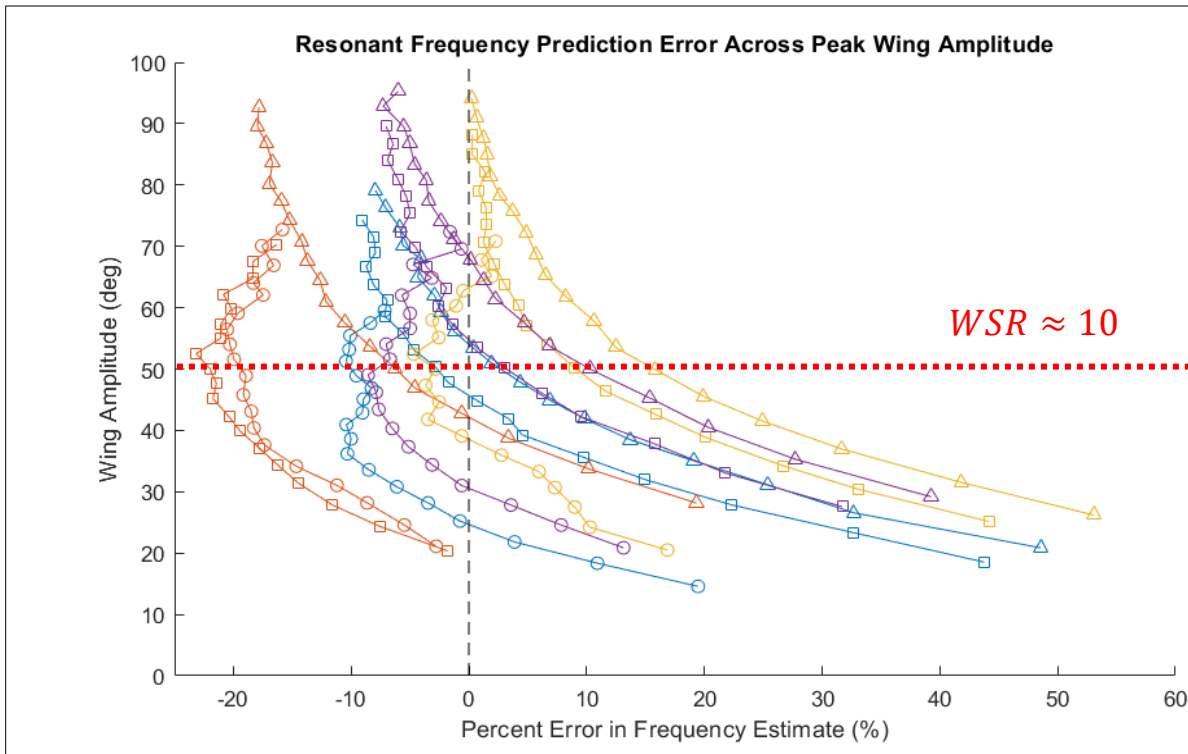

Figure 3.8: Resonant frequency prediction error with wing stroke ratio

vortex formation regime. As a result, the quasi steady estimate, which does not take into account unsteady force mechanisms, severely underestimates the transient forces. Figure 3.8 shows the resonant frequency prediction error along with a line at $WSR \approx 10$. Above that value, the error is small and independent of amplitude. Below the line, however, the error diverges as unsteady mechanisms become more significant over each cycle.

This result agrees with the findings of Altshuler et al., whose 2005 paper studying honey bee flight at low amplitudes and high frequencies also found a relationship between amplitude and prediction error from quasi-steady models [38]. Using a combination of observations of living honeybees and measurements from a dynamically-scaled robot, they found that the effects of added mass and wing-wake interactions were more significant compared to those of quasi-steady fluid loading when the wing amplitude was smallest. At large amplitudes, forces created by large-amplitude strokes were reasonably well approximated by a quasi-steady model based upon empirically measured steady-state force coefficients.

For our purposes, this means that a quasi-steady model for a series-elastic flapping wing may be reasonable for situations where wing stroke amplitude is large (>120 degrees peak-to-peak). However, if the wing amplitude is smaller or is modulated for flight control, unsteady mechanisms may become significant enough that they must be considered for the model to be reliable.

CHAPTER 4: CONCLUSIONS

We have detailed the development and implementation of a dynamically robophysical model of a series-elastic flapping wing subject to aerodynamic loading. The system features tunable system parameters, including spring stiffness and total inertia, and an actuation scheme that enables arbitrary motor input profiles.

We have performed a suite of tests across the system parameter space, varying amplitude, frequency, spring stiffness, and system inertia in order to characterize the dynamics of series-elastic wings. The data show that the resonant properties of the system depend on a combination of all of the parameters, and some qualitative features have been characterized. We also show that a simplified model of the aerodynamics of flapping wings is reasonably sufficient to predict the resonance behavior of series-elastic wings when the wings flap at high amplitudes but performs less well at low amplitudes due to the increasing influence of unsteady factors. We propose a metric, the *wing stroke ratio*, based on non-dimensional vortex formation time that may be used to evaluate the degree to which unsteady aerodynamic mechanisms contribute to forces over a cycle.

The results of this study have applications to insect biomechanics as well as to the design of flapping wing MAVs. The observation that resonant behavior depends on unsteady aerodynamic mechanisms when wings flap at low amplitudes suggests that insects with different wing stroke amplitudes may be subject to significantly different aerodynamic loading. We also observed higher amplitude gain at lower amplitudes, suggesting that insects that fly with low wing amplitudes (honeybees, mosquitos, etc) may rely on resonance more that insects with larger wing amplitudes. For roboticists, our observations suggest that the design of an FWMAV with series-elastic wing requires consideration of the regime in which it flies. When system inertias

are low compared to the drag on the wing, the resonant frequency depends on the wing amplitude. Additionally, the amplitude gain will change as the amplitude and frequency of the actuator change, so control of such a vehicle will need to take into consideration the wing amplitude bandwidth for that particular system.

REFERENCES

[1] M. H. Dickinson, F. O. Lehmann, and S. P. Sane, "Wing Rotation and the Aerodynamics Basis of Insect Flight," *Science*, vol. 284, no. June, pp. 1954–1960, 1999.

[2] K. G. Götz, "Course-Control, Metabolism and Wing Interference During Ultralong Tethered Flight in Drosophila Melanogaster," *J. Exp. Biol.*, vol. 128, no. 1, pp. 35–46, Mar. 1987.

[3] K. Y. Ma, P. Chirarattananon, S. B. Fuller, and R. J. Wood, "Controlled flight of a biologically inspired, insect-scale robot," *Science*, vol. 340, no. 6132, pp. 603–607, 2013.

[4] K. Y. Ma, P. Chirarattananon, and R. J. Wood, "Design and fabrication of an insect-scale flying robot for control autonomy," *IROS*, pp. 1558–1564, 2015.

[5] M. Karásek, F. T. Muijres, C. De Wagter, B. D. W. Remes, and G. C. H. E. de Croon, "A tailless aerial robotic flapper reveals that flies use torque coupling in rapid banked turns," *Science*, vol. 361, no. 6407, pp. 1089–1094, Sep. 2018.

[6] M. Keennon, K. Klingebiel, and H. Won, "Development of the Nano Hummingbird: A Tailless Flapping Wing Micro Air Vehicle," presented at the 50th AIAA Aerospace Sciences Meeting, Nashville, Tennessee, 2012.

[7] A. Roshanbin, H. Altartouri, M. Karásek, and A. Preumont, "COLIBRI: A hovering flapping twin-wing robot," *Int. J. Micro Air Veh.*, vol. 9, no. 4, pp. 270–282, 2017.

[8] K. E. Machin and J. W. S. Pringle, "The physiology of insect fibrillar muscle - II Mechanical properties of a beetle flight muscle," *Proc. R. Soc. Lond. B Biol. Sci.*, vol. 151, no. 943, pp. 204–225, Dec. 1959.

[9] R. M. N. Alexander, "Springs for Wings," *Science*, vol. 268, no. 5207, p. 50, 1995.

[10] C. H. Greenewalt, "The Wings of Insects and Birds as Mechanical Oscillators," *Proc. Am. Philos. Soc.*, vol. 104, no. 6, pp. 605–611, 1960.

[11] T. Weis-Fogh, "A Rubber-like Protein in Insect Cuticle," p. 21, 1960.

[12] M. Jensen and T. Weis-Fogh, "Biology and physics of locust flight. V. Strength and elasticity of locust cuticle," *Philos. Trans. R. Soc. Lond. B. Biol. Sci.*, vol. 245, no. 721, pp. 137–169, Oct. 1962.

[13]   H. Bennet-Clark, "The First Description of Resilin," *J. Exp. Biol.*, vol. 210, no. 22, pp. 3879–3881, Nov. 2007.

[14]   C. Zhang and C. Rossi, "A review of compliant transmission mechanisms for bio-inspired flapping-wing micro air vehicles," *Bioinspir. Biomim.*, vol. 12, no. 2, p. 025005, Feb. 2017.

[15]   M. B. BENNETT, R. F. KER, and R. M. ALEXANDER, "Elastic properties of structures in the tails of cetaceans (Phocaena and Lagenorhynchus) and their effect on the energy cost of swimming," *J. Zool.*, 1987.

[16]   R. M. N. Alexander, "Springs as Energy Stores: Swimming and Flight," in *Principles of Animal Locomotion*, Princeton University Press, 2003, pp. 51–71.

[17]   D. O. Sotavalta, "Flight-Tone and Wing-Stroke Frequency of Insects and the Dynamics of Insect Flight," p. 2, 1952.

[18]   D. M. Unwin and S. A. Corbet, "Wingbeat frequency, temperature and body size in bees and flies," *Physiol. Entomol.*, vol. 9, no. 1, pp. 115–121, Mar. 1984.

[19]   L. Hines, D. Campolo, and M. Sitti, "Liftoff of a motor-driven, flapping-wing microaerial vehicle capable of resonance," *IEEE Trans. Robot.*, vol. 30, no. 1, pp. 220–232, 2014.

[20]   S. S. Baek, K. Y. Ma, and R. S. Fearing, "Efficient resonant drive of flapping-wing robots," in *2009 IEEE/RSJ International Conference on Intelligent Robots and Systems*, St. Louis, MO, USA, 2009, pp. 2854–2860.

[21]   R. Sahai, K. C. Galloway, and R. J. Wood, "Elastic element integration for improved flapping-wing micro air vehicle performance," *IEEE Trans. Robot.*, vol. 29, no. 1, pp. 32–41, 2013.

[22]   W. Bejgerowski, J. W. Gerdes, S. K. Gupta, and H. A. Bruck, "Design and fabrication of miniature compliant hinges for multi-material compliant mechanisms," *Int. J. Adv. Manuf. Technol.*, vol. 57, no. 5–8, pp. 437–452, Nov. 2011.

[23]   T. Weis-Fogh, "ENERGETICS OF HOVERING FLIGHT IN HUMMINGBIRDS AND IN DROSOPHILA," *J. Exp. Biol.*, vol. 56, p. 26, 1972.

[24]   T. Weis-Fogh, "QUICK ESTIMATES OF FLIGHT FITNESS IN HOVERING ANIMALS, INCLUDING NOVEL MECHANISMS FOR LIFT PRODUCTION," *J. Exp. Biol.*, vol. 59, p. 62, 1973.

[25]   C. P. Ellington, "THE AERODYNAMICS OF HOVERING INSECT FLIGHT: 1. THE QUASI-STEADY ANALYSIS," *Philos. Trans. R. Soc. Lond. B Biol. Sci.*, 1984.

[26]   C. P. Ellington, "THE AERODYNAMICS OF HOVERING INSECT FLIGHT: 2. MORPHOLOGICAL PARAMETERS," *Philos. Trans. R. Soc. Lond. B Biol. Sci.*, 1984.

[27]   C. P. Ellington, "THE AERODYNAMICS OF HOVERING INSECT FLIGHT: 3. KINEMATICS," *Philos. Trans. R. Soc. Lond. B Biol. Sci.*, 1984.

[28]   C. P. Ellington, "THE AERODYNAMICS OF HOVERING INSECT FLIGHT: 4. AERODYNAMIC MECHANISMS," *Philos. Trans. R. Soc. Lond. B Biol. Sci.*, 1984.

[29]   C. P. Ellington, "THE AERODYNAMICS OF HOVERING INSECT FLIGHT: 5. A VORTEX THEORY," *Philos. Trans. R. Soc. Lond. B Biol. Sci.*, 1984.

[30]   C. P. Ellington, "THE AERODYNAMICS OF HOVERING INSECT FLIGHT: 6. LIFT AND POWER REQUIREMENTS," *Philos. Trans. R. Soc. Lond. B Biol. Sci.*, 1984.

[31]   D. D. Chin and D. Lentink, "Flapping wing aerodynamics: from insects to vertebrates," *J. Exp. Biol.*, vol. 219, no. 7, pp. 920–932, 2016.

[32]   S. P. Sane, "The aerodynamics of insect flight," *J. Exp. Biol.*, vol. 206, no. 23, pp. 4191–4208, Dec. 2003.

[33]   S. P. Sane and M. H. Dickinson, "The Control of Flight Force by a Flapping Wing: Lift and Drag Production," *J. Exp. Biol.*, vol. 204, p. 20, 2001.

[34]   S. P. Sane and M. H. Dickinson, "The aerodynamic effects of wing rotation and a revised quasi-steady model of flapping flight," p. 10, 2002.

[35]   C. van den Berg and C. P. Ellington, "The vortex wake of a 'hovering' model hawkmoth," *Philos. Trans. R. Soc. Lond. B. Biol. Sci.*, vol. 352, no. 1351, pp. 317–328, Mar. 1997.

[36]   J. Han, Z. Yuan, and G. Chen, "Effects of kinematic parameters on three-dimensional flapping wing at low Reynolds number," *Phys. Fluids*, vol. 30, no. 8, 2018.

[37]   J. O. Dabiri, "Optimal Vortex Formation as a Unifying Principle in Biological Propulsion," *Annu. Rev. Fluid Mech.*, vol. 41, no. 1, pp. 17–33, 2009.

[38]   D. L. Altshuler, W. B. Dickson, J. T. Vance, S. P. Roberts, and M. H. Dickinson, "Short-amplitude high-frequency wing strokes determine the aerodynamics of honeybee flight," *Proc. Natl. Acad. Sci.*, vol. 102, no. 50, pp. 18213–18218, Dec. 2005.